Reduction in ETFDH expression optimizes cancer cell bioenergetics

David Papadopoli[1,2], Ranveer Palia[1,3], Predrag Jovanovic[1,3], Sébastien Tabariès[4], Emma Ciccolini[1,3], Valerie Sabourin[1], Sebastian Igelmann[5], Shannon McLaughlan[1], Lesley Zhan[1,6], HaEun Kim[1,3], Nabila Chekkal[1,6], Krzysztof J. Szkop[7], Thierry Bertomeu[8], Jibin Zeng[1], Julia Vassalakis[9], Farzaneh Afzali[9], Slim Mzoughi[10], Ernesto Guccione[10], Mike Tyers[11], Daina Avizonis[4,12], Ola Larsson[7], Lynne-Marie Postovit[9], Sergej Djuranovic[13], Josie Ursini-Siegel[1,2,3,6], Peter M. Siegel[3,4,6], Michael Pollak[1,2,3*], Ivan Topisirovic[1,2,3,6,14*]

[1]Lady Davis Institute, SMBD JGH, McGill University, Montréal, QC H3T 1E2, Canada.

[2]Gerald Bronfman Department of Oncology, McGill University, Montréal, QC H3A 0G4, Canada.

[3]Department of Experimental Medicine, McGill University, Montréal, QC H3A 0G4, Canada.

[4]Rosalind and Morris Goodman Cancer Institute, McGill University, Montréal, QC H3A 1A3, Canada

[5]VIB Center for Cancer Biology, Department of Oncology, KU Leuven and Leuven Cancer Institute (LKI), Herestraat 49, 3000 Leuven, Belgium.

[6]Department of Biochemistry, McGill University, Montréal, QC H3A 0G4, Canada.

[7]Department of Oncology-Pathology, Science for Life Laboratory, Karolinska Institute, 171 77, Stockholm, Sweden.

[8]Institute for Research in Immunology and Cancer, Université de Montréal, Montréal, QC H3T 1J4, Canada.

[9]Department of Biomedical and Molecular Sciences, Queen's University, Kingston, ON K7L 3N6, Canada.

[10]Center of OncoGenomics and Innovative Therapeutics (COGIT), Department of Oncological Sciences, Tisch Cancer Institute, Icahn School of Medicine at Mount Sinai, New York, NY, 10029 United States

[11]Program in Molecular Medicine, The Hospital for Sick Children, Toronto, ON M5G 0A4, Canada. Department of Molecular Genetics, University of Toronto, Toronto, ON M5S 1A8, Canada.

[12]Metabolomics Innovation Resource, McGill University, Montréal, QC, Canada.

[13]Department of Cell Biology and Physiology, Washington University School of Medicine, St. Louis, MO 63110, United States

[14]Lead Contact

[*]Correspondence michael.pollak@mcgill.ca (M.P.), ivan.topisirovic@mcgill.ca (I.T.)

Keywords: Electron transfer flavoprotein dehydrogenase (ETFDH), cancer metabolism, mRNA translation, mechanistic target of rapamycin (mTOR), 4E-binding protein 1 (4E-BP1).

Summary

Cancer cells reprogram their metabolism to meet the energy demands of neoplasia. We observed that the level of expression of mitochondrial enzyme electron transfer flavoprotein dehydrogenase (ETFDH) is unexpectedly decreased in most human malignancies relative to that in tissue-of-origin. Reduced ETFDH expression increases proliferation and neoplastic growth *in vivo*. This is a consequence of intracellular accumulation of amino acids leading to the activation of mTORC1, increase in B-cell lymphoma 6 (*BCL-6)* levels, and BCL-6-dependent suppression of the eukaryotic translation initiation factor 4E-binding protein 1 (*EIF4EBP1*) transcription. 4E-BP1 downregulation and mTORC1 hyperactivation increase mitochondrial biogenesis, function, and

bioenergetic capacity thereby outweighing the advantage of flexibility in OXPHOS substrate utilization. Thus, the level of ETFDH expression plays a critical role in regulating trade-offs to optimize energy metabolism and coordinate it with signaling perturbations in cancer cells.

Introduction

Tumors rapidly outstrip their nutrient supply during neoplastic growth [1]. Therefore, cancer cells adapt to constant fluctuations in nutrient and oxygen availability to support their energetic and biosynthetic needs [1,2]. Emerging data show that cancer cells exhibit metabolic plasticity to adapt to stress emanating from their microenvironment, which allows them to metastasize and oppose therapeutic insults [3]. Elucidating molecular mechanisms that govern metabolic plasticity in cancer is the first step towards therapeutically exploiting metabolic vulnerabilities [4].

Cancer cells rely on mitochondrial bioenergetics and catabolism of multiple fuels, including glucose, amino acids, and fatty acids [5]. The mitochondrial electron transport chain (ETC) transfers high-energy electrons from reducing equivalents (NADH and $FADH_2$) towards complexes I/II, or from peripheral metabolic enzymes that reduce coenzyme Q (ubiquinone, Q) to ubiquinol (QH_2) [6]. The electron transfer flavoproteins (ETF, including ETFA and ETFB) accept electrons generated by the catabolism of branched-chain amino acids and fatty acids [7-9]. ETFs interact with ETF dehydrogenase (ETFDH or ETF-ubiquinone oxidoreductase)[10], which controls electron flow towards complex III of the ETC [11]. Loss-of-function mutations in ETF/ETFDH occur in metabolic diseases such as multiple acyl-CoA dehydrogenase deficiency (MADD) [12,13]. More recently, ETFDH has been shown to play a prominent role in skeletal muscle cell function [11].

Notwithstanding that ETFDH acts at the intersection of the ETC and metabolic pathways implicated in cancer cell plasticity, its function(s) in neoplasia have not been explored. We show that ETFDH expression is reduced across human neoplasia and that its reduced expression

accelerates neoplastic growth *in vitro* and *in vivo*. ETFDH disruption in cancer cells leads to enhanced mitochondrial biogenesis and hyperfunction, thus increasing bioenergetic capacity, which occurs via accumulation of intracellular amino acids, increased mTOR activity and BCL-6 mediated decrease in 4E-BP1 levels. These data demonstrate that reduction in ETFDH levels serves as a tradeoff, whereby alterations in cellular ability to feed ETC is compensated by retrograde signaling programs that optimize cancer cell bioenergetics to support neoplastic growth.

Results

ETFDH expression is reduced in cancer cells and its absence promotes tumor growth

ETFDH functions as a facultative contributor of electrons to the ETC [6] (Fig.S1A). Using publicly available cancer patient databases, we observed reduction in *ETFDH* mRNA levels across all tested human cancer types, including colon (Fig.S1B) and breast cancer (Fig.S1C). *ETFDH* expression also associates with clinical outcome, as low *ETFDH* mRNA levels are correlated with poor patient survival in colon (Fig.S1D) and breast cancer (Fig.S1E). To confirm that the ETFDH protein levels mirror downregulation of corresponding mRNA levels, we carried out immunohistochemistry (IHC) staining on tumor microarrays (TMAs). This confirmed that ETFDH protein levels are significantly reduced in colorectal cancer vs. non-adjacent patient-derived tissues (NAT) (Fig.1A). Considering its frequent downregulation across a spectrum of different neoplasia, we next addressed the essentiality of ETFDH in cancer cells. In stark contrast to skeletal muscle cells [11], a CRISPR-Cas9 KO screen performed in a human acute lymphoblastic leukemia cell line (NALM6) [14] revealed *ETFDH* as a top non-essential gene, whose rank score clustered along-side well-established tumor suppressor genes including *TP53* and *RB1* (Fig.S1F). Based on the observations that *ETFDH* expression is downregulated across different cancer types, and that *ETFDH* clusters with non-essential, tumor suppressive genes in NALM6 cells, we next sought to

establish whether the ETFDH status in the cell affects neoplastic growth. To achieve this, we first abrogated the *ETFDH* gene using a CRISPR-Cas9 approach in a variety of cell lines established from cancers originating from different tissues. This included HCT-116 (human colorectal cancer), NT2197 (murine HER2+ breast cancer), 4T1 (murine triple negative breast cancer cells), and NALM6 cells (Fig.S1G-J). In addition, we investigated the effects of ETFDH loss in non-transformed normal murine mammary gland (NMuMG) cells (Fig.S1K) that represent parental immortalized mammary epithelial cells that were transformed with an oncogenic ErbB2 variant to generate NT2197 cell line [15]. Notwithstanding that selected cancer cell lines are highly proliferative, ETFDH ablation significantly increased proliferation across all tested cancer cell lines (Fig.S1G-J). To confirm that these effects were due to ETFDH loss, and not due to potential inadvertent effects of the CRISPR-Cas9 approach, we rescued ETFDH expression in HCT-116 and NT2197 cells, which reverted the effects of ETFDH loss by reducing proliferation rates to levels comparable to ETFDH-proficient control cells (Fig.S1G-H). In contrast, ETFDH abrogation in non-transformed NMuMG cells did not exert a major effect on proliferation (Fig.S1K). Collectively, these data show that the loss of ETFDH increases proliferation rates across a variety of cancer cell lines, without having a major effect on proliferation in a non-transformed epithelial type. We next investigated whether the loss of ETFDH stimulates anchorage-independent growth in soft agar, which is a surrogate measurement of cellular neoplastic potential [16]. Consistent with observations in proliferation assays, ETFDH KO cells more efficiently form colonies in soft agar as compared to ETFDH-proficient empty vector controls (WT EV), and ETFDH-deficient cells with rescued expression of ETFDH (ETFDH Rescue) in HCT-116 (Fig.S1L) and NT2197 (Fig.S1M) cell lines.

Based on these findings, we tested the impact of ETFDH loss on neoplastic growth *in vivo.* To achieve this, WT EV, ETFDH KO, or ETFDH Rescue HCT-116 cells were injected

orthotopically in the caeca of SCID-BEIGE mice. Loss of ETFDH significantly increased the tumor growth rate, leading to a larger tumor volume at endpoint relative to ETFDH-proficient controls, while ETFDH re-expression in ETFDH KO cells reversed both parameters (Fig.1B-C). ETFDH loss also increased NT2197 tumor growth and the final tumor volume as compared to ETFDH-proficient tumors following orthotopic mammary fat pad injections in SCID-BEIGE mice (Fig.1D-E). Taken together, these results show that *ETFDH* expression is decreased across a wide spectrum of cancer types, whereby ETFDH loss bolsters neoplastic growth, while seemingly not having a major impact on proliferation of non-transformed cells.

ETFDH loss remodels mitochondrial metabolism and increases bioenergetic capacity

In non-cancerous cells, ETFDH transfers electrons from catabolism of fatty acids and amino acids to the ETC (Fig.S2A). To confirm the functional impact of ETFDH ablation on fatty acid consumption in cancer cells, palmitate oxidation was monitored in ETFDH-proficient empty vector (WT EV), deficient (ETFDH KO) or rescued (ETFDH Rescue) HCT-116 cells. As expected, palmitate oxidation (monitored by oxygen consumption) was strongly attenuated by ETFDH abrogation (Fig.S2B). We also monitored the effects of ETFDH loss on leucine catabolism by measuring the labelling of citrate m+2 following incorporation of ^{13}C-labelled leucine. ETFDH KO HCT-116 cells exhibited decreased tracing of ^{13}C labelling into citrate (citrate m+2), as compared to WT EV and ETFDH Rescue HCT-116 cells (Fig.S2C). These data show that the role of ETFDH in the breakdown of lipids and amino acids via acyl-CoA metabolism is preserved in cancer cells [17]. Given that we established that ETFDH loss bolsters neoplastic growth (Fig.1B-E), while mitochondrial metabolism is well-established in fueling tumor growth [5], we next carried out bioenergetic analyses of WT EV, ETFDH KO and ETFDH rescue HCT-116 cells in full culture media (see STAR Methods). Surprisingly, ETFDH loss increased oxygen consumption and

extracellular acidification in HCT-116 cells, which was restored to control WT cell levels upon ETFDH rescue (Fig.2A-B). Notably, ETFDH KO HCT116 cells produced higher levels of ATP from oxidative phosphorylation (*J* ATP ox) as compared to ETFDH-proficient cells (Fig 2C-D). Consequently, ETFDH loss increased the bioenergetic capacity of HCT-116 cells (Fig.2E). Comparable results were observed in ETFDH-proficient and deficient NT2197 cells (Fig.S2D-H). Collectively, these findings suggest that notwithstanding that ETFDH transfers electrons to the ETC, its loss paradoxically upregulates mitochondrial metabolism and bioenergetic capacity.

Glutamine plays an important anaplerotic role in fueling mitochondrial metabolism in cancer cells [18]. ETFDH abrogation increased glutamine uptake and glutamate production in both HCT-116 (Fig.2F) and NT2197 (Fig.S2I) cells. To further establish the impact of glutamine on replenishing the citric acid cycle (CAC) as a function of the ETFDH status in the cell, ^{13}C-glutamine tracing was performed, and ^{13}C-labelled metabolites (glutamate, proline, succinate, fumarate, malate, aspartate, and citrate) were measured (Fig.2G). ETFDH loss in HCT-116 and NT2197 increased glutamine incorporation in the forward direction (green) and the reverse direction (purple) of the citric acid cycle (CAC; Fig.2H, Fig.S2J), suggesting higher glutamine utilization in the CAC, as well as increased reductive glutamine metabolism. Accordingly, ETFDH KO HCT-116 cells exhibited greater sensitivity to glutamine deprivation than control WT EV cells (Fig.2I). These findings thus show that ETFDH loss elevates glutamine utilization in the CAC to support mitochondrial metabolism. Collectively, these data demonstrate that the loss of ETFDH remodels mitochondrial metabolism while increasing the bioenergetic capacity of cancer cells.

ETFDH loss induces intracellular accumulation of amino acids, mTOR signaling and protein synthesis

We next sought to dissect the mechanisms that underpin the role of ETFDH in suppressing tumor growth and remodeling of cancer cell bioenergetics. Considering the established role of ETFDH in amino acid catabolism [7], and the observed reduction of leucine consumption in the CAC upon ETFDH abrogation (Fig.S2C), we next monitored the impact of ETFDH loss on intracellular amino acid levels. These experiments revealed an increase in steady state levels of most intracellular amino acids in ETFDH KO vs. WT HCT116 and NT2197 cells (Fig.3A). Notably, ETFDH loss induced a prominent increase in the intracellular branched-chain amino acids (BCAAs) levels (Fig.3A). To establish the functional significance of increased amino acid levels, global protein synthesis was monitored in ETFDH-deficient and proficient cells. This revealed that ETFDH-deficient HCT-116 cells have higher rates of protein synthesis relative to ETFDH-proficient cells (Fig.3B). Given that BCAAs act as potent activators of the mechanistic target of rapamycin (mTOR) and that mTOR stimulates protein synthesis [19], we next investigated whether the loss of ETFDH affects mTOR signaling. These experiments revealed that mTORC1 signaling is higher in ETFDH-deficient than ETFDH-proficient cells as illustrated by increased phosphorylation of ribosomal protein S6 kinases (S6K1/2; Thr389) and their substrate ribosomal protein S6 (rpS6; Ser240/244) in HCT-116 and NT2197 cells (Fig.3C). Re-expression of ETFDH in ETFDH KO HCT-116 and NT2197 cells resulted in normalization of mTORC1 signaling to the levels observed in WT EV cells (Fig 3D). Moreover, we observed an increase in mTORC2 signaling in ETFDH KO cells as evidenced by increased AKT phosphorylation (Ser473) in KO cells compared to controls in HCT-116 and NALM6 cells (Fig.S3A-B). Despite bioenergetic rewiring, ETFDH loss did not exert a major effect on the activity of adenosine monophosphate-

activated protein kinase (AMPK; Thr172) as monitored by its phosphorylation or phosphorylation of its substrate Acetyl-CoA carboxylase (ACC at S79) (Fig. S3A-B).

We next explored whether the increase in mTOR signaling contributes to the hyper-proliferative phenotype caused by ETFDH loss. ETFDH KO HCT-116 cells demonstrated increased sensitivity to the active site mTORC1/2 inhibitor Torin1 [20] as compared to their ETFDH-proficient counterparts (Fig.S3F). To further determine which mTOR complex is responsible for mediating the hyper-proliferative phenotype triggered by ETFDH loss, we selectively inactivated mTORC1 or mTORC2 by depleting RAPTOR or RICTOR, respectively using small hairpin RNA (shRNA) in WT and ETFDH KO HCT-116 cells (Fig.S3C). Depletion of RAPTOR, but not RICTOR strongly attenuated the proliferation of ETFDH KO cells (Fig.S3D-E). Moreover, the anti-proliferative effects of bisteric mTORC1-specific inhibitor BiS-35x [21] where significantly more pronounced in ETFDH KO vs. ETFDH Rescue HCT-116 cells (Fig.S3G). Altogether, these data suggest that mTORC1, but not mTORC2, acts as a major mediator of hyper-proliferative phenotype triggered by ETFDH loss in cancer cells.

Next, we investigated whether the intracellular amino acid accumulation caused by abrogation of ETFDH is indeed responsible for the observed increase in mTORC1 signaling. To achieve this, ETFDH-proficient or ETFDH-deficient HCT116 cells were deprived of amino acids. The effects of amino acid deprivation on phospho-rpS6 (Ser240/244), and phospho-4E-BP1 (Ser 65) were attenuated in ETFDH KO vs. WT control cells, which is consistent with the intracellular accumulation of amino acids upon ETFDH disruption (Fig.3E-G). In turn, serum stimulation (Stim) resulted in comparable induction in phosphorylation of rpS6 (Ser240/244) and 4E-BP1 (Ser65) in ETFDH-deficient and proficient cells (Fig.3E-G). Collectively, these findings suggest that ETFDH loss induces mTORC1 signaling at least in part by increasing intracellular amino acid levels.

Amino acid deprivation leads to general control nonderepressible 2 (GCN2)-dependent phosphorylation of the alpha subunit of eIF2 and subsequent induction of activating transcription factor 4 (ATF4) synthesis during integrated stress response (ISR) [22]. Consistent with an increase in intracellular amino acid, phosho-eIF2α (S51) levels appeared to be slightly lower in ETFDH-deficient vs. proficient HCT-116 cells under both serum starvation and amino acid depletion (Fig.S3H). However, the ETFDH status in the cells did not appear to exert a noticeable effect on ATF4 levels at the baseline or upon amino acid depletion (Fig.S3H). Altogether, these data demonstrate that ETFDH loss induces mTORC1 signaling and protein synthesis, which is driven by intracellular accumulation of amino acids. In turn, loss of ETFDH does not appear to exert major effect on AMPK signaling or ISR.

ETFDH loss diminishes 4E-BP1, but not 4E-BP2 protein levels

mTORC1 positively controls cell proliferation through eukaryotic translation initiation factor 4E-binding proteins (4E-BPs; 4E-BP1-3 in mammals) [23]. Of note, 4E-BP3 is expressed in a tissue-restricted manner, and does not appear to play a major role in regulating proliferation downstream of mTORC1 [23]. mTORC1 phosphorylates 4E-BPs to promote eukaryotic translation initiation factor 4F (eIF4F) complex assembly by dissociating 4E-BPs from eIF4E, thereby stimulating cap-dependent translation initiation [24]. Consistent with the increased mTORC1 activity, ETFDH-deficient cells exhibited increased phosphorylation of 4E-BP1 (Ser65), which was rescued upon re-expression of ETFDH in HCT-116 and NT2197 cells (Fig.4A). Unexpectedly, however, we observed that ETFDH loss coincided with a dramatic reduction in total 4E-BP1 protein levels in HCT-116 (Fig.4A), NT2197 (Fig.4A), NALM6 (Fig.S4A), and 4T1 cells (Fig.S4B). To exclude the possibility that the differences in phosphorylation state may confound interpretation of the effects of ETFDH loss on 4E-BP1 protein abundance, we treated lysates obtained from HCT-116

ETFDH WT and KO cells with λ-phosphatase to completely dephosphorylate 4E-BP1 (Fig.4B). These experiments confirmed that the 4E-BP1 protein levels are indeed reduced in ETFDH-deficient vs. ETFDH-proficient cells. Re-expression of ETFDH in ETFDH-deficient HCT-116 and NT2197 cells restored 4E-BP1 levels to those observed in control WT ETFDH cells (Fig.4A). Notably, loss of ETFDH did not exert a major effect on 4E-BP2 protein abundance in HCT-116 (Fig.4A), NT2197 (Fig.4A), or 4T1 cells (Fig.S4B). In addition, 4E-BP1 protein levels were reduced in ETFDH-deficient HCT-116 tumors as compared to their WT counterparts (Fig.4C-D). Consistently, 4E-BP2 protein levels did not change in HCT-116 WT and ETFDH KO tumors (Fig.4C, E). In contrast to cancer cells, loss of ETFDH in non-transformed NMuMG cells did not exert a major effect on mTORC1 signaling, as monitored by phosphorylation of rpS6 (Ser240/244) (Fig.S4C) and failed to alter 4E-BP1 protein levels (Fig.S4C). Collectively, these findings indicate that the loss of ETFDH is paralleled by a prominent decrease in 4E-BP1, but not 4E-BP2 protein levels in cancer cells.

<u>Decrease in 4E-BP1 protein levels underpins the bioenergetic rewiring and pro-tumorigenic effects caused by ETFDH disruption.</u>

Considering that in mammals 4E-BPs play a major role in mediating the effects of mTORC1 on proliferation, neoplastic growth, mitochondrial functions and protein synthesis [4,23,25], we next investigated whether the observed decrease in 4E-BP1 levels contributes to increased proliferation and tumor growth caused by abrogation of ETFDH. To determine whether the effects of ETFDH loss on bioenergetic rewiring and neoplastic growth can be attributed to a decrease in 4E-BP1 protein levels, we overexpressed 4E-BP1 protein in ETFDH-deficient NT2197 cells by infecting them with a retrovirus wherein *EIF4EBP1* expression was driven by exogenous promoter [23]. Importantly, 4E-BP1 overexpression in ETFDH KO NT2197 cells decreased eIF4F complex

assembly, as evidenced by reduced eIF4G1 and increased 4E-BP1 amount in the material pulled down by m^7-GTP cap analogue as compared to control, empty vector expressing ETFDH KO NT2197 cells (Fig.4F). 4E-BP1 overexpression also reduced oxygen consumption in ETFDH KO NT2197 cells, relative to empty vector infected cells (Fig.4G). Moreover, restoring 4E-BP1 protein levels decreased cell proliferation (Fig.S4D) and anchorage-independent growth (Fig.S4E) of ETFDH KO HCT-116 cells. Lastly, 4E-BP1 overexpression decreased growth and the final volume of tumors formed by ETFDH NT2197 KO cells (Fig.4H-I). Collectively, these data indicate that decreased 4E-BP1 protein levels play a major role in mediating the pro-neoplastic effects of ETFDH loss.

The mTORC1/4E-BP axis plays a major role in reprogramming mitochondrial biogenesis and metabolism in large part by altering the translation of nuclear-encoded mitochondrial mRNAs including mitochondrial transcription factor A (TFAM) which acts as a master orchestrator of mitochondrial gene expression and biogenesis [25,26]. Considering that we observed an increase in mitochondrial DNA levels (Fig.4J) and mitochondrial mass (Fig.S4F) upon ETFDH loss, we next assessed the potential role of the mTORC1/4E-BP axis in mediating these effects. Consistent with decreased 4E-BP1 levels and an increase in mTORC1 signaling, ETFDH-deficient HCT-116 cells exhibited increased levels of TFAM protein as compared to the control ETFDH WT EV cells, which was reverted by rescuing ETFDH expression (Fig.4K). Collectively, these data show that the loss of 4E-BP1 plays a prominent role in mediating the pro-tumorigenic effects of ETFDH abrogation, whereby the effects on bioenergetic reprogramming are likely mediated by the ETFDH-driven perturbations of signaling via the mTORC1/4E-BP axis.

ETFDH loss decreases *EIF4EBP1* transcription.

Thus far, we established that abrogating ETFDH expression is paralleled by a decrease in 4E-BP1 protein levels, which bolsters neoplastic growth. Next, we set out to determine the level(s) at which 4E-BP1 expression is downregulated upon ETFDH loss. We first monitored the effects of ETFDH loss on the stability of 4E-BP1 protein. To this end, WT and ETFDH KO HCT-116 cells were treated with the translation inhibitor cycloheximide (CHX) (50μg/ml) for 2 hours, the proteasomal inhibitor MG-132 (10μM) for 2 hours, and the combination thereof for 4 hours total (Fig. S4G). Blocking protein synthesis did not further reduce 4E-BP1 protein levels, whereas proteasome inhibition failed to increase 4E-BP1 protein abundance in ETFDH KO relative to ETFDH-proficient cells (Fig. S4G). This indicated that the differences in 4E-BP1 protein levels between ETFDH-deficient vs. proficient cells are unlikely to stem from the alterations in protein stability. We next assessed the effects of ETFDH loss on *EIF4EBP1* mRNA translation using polysome profiling (Fig. S4H). ETFDH deletion coincided with a decrease in the 80S monosome peak and a concomitant increase in the polysomes, thereby supporting that ETFDH loss enhances global protein synthesis (Fig.S4H). However, ETFDH disruption did not affect the distribution of *EIF4EBP1* mRNA across the gradient, thereby demonstrating that *EIF4EBP1* mRNA translation is not affected by the ETFDH status in the cell (Fig.S4H). Conversely, we noted that the abundance of *EIF4EBP1* mRNA is decreased in ETFDH-deficient vs. ETFDH-proficient HCT-116 (Fig.4L) and NT2197 cells (Fig.4M). *EIF4EBP1* and *ETFDH* mRNA were also positively correlated in tumors isolated from colorectal adenocarcinoma patients (Fig.S4I). Taken together, these data suggest that ETFDH abrogation decreases *EIF4EBP1* mRNA levels. In turn, consistent with no apparent differences in 4E-BP2 protein levels, the levels of *EIF4EBP2* mRNA were unaffected by the ETFDH status in both cell lines (Fig.4L-M). To decipher whether the observed decrease in

EIF4EBP1 mRNA levels triggered by ETFDH loss stem from the changes in mRNA stability, we treated ETFDH WT or KO HCT-116 cells with the transcriptional inhibitor Actinomycin D (ActD). ActD treatment resulted in a comparable decrease in *EIF4EBP1* mRNA levels in both cell lines over time, thus suggesting that *EIF4EBP1* mRNA stability is unlikely to be affected by the ETFDH status in the cell (Fig.S4J). Based on these data, we concluded that ETFDH abrogation is paralleled by suppression of *EIF4EBP1* transcription.

BCL-6 levels are increased in ETFDH deficient cells and BCL-6 represses *EIF4EBP1* transcription.

We next decided to pursue the mechanisms underpinning the transcriptional repression of *EIF4EBP1* in ETFDH KO cells. Herein, we sought to identify transcription factors that mediate the effects of ETFDH abrogation on suppression of *EIF4EBP1* expression. ATF4 has been shown to stimulate transcription of *EIF4EBP1*, but not *EIF4EBP2*, under ER stress [27]. However, ATF4 protein levels remain unchanged upon ETFDH perturbation (Fig.S3H). Furthermore, Snail and Slug have been reported to act as transcriptional repressors of *EIF4EBP1* in breast, colon, and lung cancer cell lines, without affecting other 4E-BP family members [28]. Nonetheless, both Snail and Slug protein abundances were unaffected by ETFDH status in HCT-116 cells (Fig.S5A). We also re-analyzed publicly available RNA-seq datasets, which revealed that *EIF4EBP1*, but not *EIF4EBP2* expression were increased following STAT1 abrogation in MT4788 breast cancer cells [29]. Indeed, we observed that MT4788 STAT1 KO cells have increased 4E-BP1 protein levels relative to parental cells (Fig.S5B). Accordingly, ETFDH KO cells displayed increased STAT1 and downregulated 4E-BP1 protein levels (Fig.S5C). To determine the impact of STAT1 on *EIF4EBP1* or *EIF4EBP2* promoter occupancy, we performed chromatin immunoprecipitation qPCR (ChIP-qPCR) assay in control (WT EV), ETFDH KO, or ETFDH rescue HCT-116 cells

(Fig.S5D-E). Binding of STAT1 was however comparable to IgG across all tested cell lines thereby suggesting that is unlikely that STAT1 directly suppresses *EIF4EBP1* transcription in the context of ETFDH loss (Fig.S5D-E). Furthermore, reactive oxygen species (ROS) can also influence redox-responsive transcription [30]. Although loss of ETFDH induced ROS levels (Fig.S5F), 4E-BP1 protein abundance was not altered following treatment with the antioxidant N-acetyl-cysteine (NAC) (Fig.S5G). Taken together, decreased *EIF4EBP1* expression does not appear to be directly mediated by several previously reported *EIF4EBP1* transcriptional regulators including ATF4, Snail, Slug, or STAT1, nor by ROS.

Therefore, we next investigated the potential role of B-cell lymphoma 6 (BCL-6) [31-33], which has recently been shown to suppress *EIF4EBP1* transcription [34]. Notably, ETFDH abrogation in HCT-116 and NT2197 cells resulted in a marked increase in BCL-6 protein levels, compared to ETFDH-proficient control cells (Fig.5A). These changes in BCL-6 protein levels were not accompanied by the alterations in corresponding mRNA abundance (Fig.5B), thereby suggesting that abrogation of ETFDH does not affect BCL-6 expression at the transcriptional level. BCL-6 was shown to be translationally induced by mTOR [35-37]. To this end, we treated ETFDH KO NT2197 cells with Torin1 which strongly reduced BCL-6 levels as compared to a vehicle treated control cells (Fig.5C). Taken together, these data point out that ETFDH disruption post-transcriptionally induces BCL-6 via mTOR.

Next, ChIP-qPCR was performed to determine the functional role of BCL-6 on transcription upon ETFDH loss. ETFDH KO cells displayed increased binding of BCL-6 to the *EIF4EBP1* promoter (Fig.5D). In contrast, the binding of BCL-6 to the *EIF4EBP2* promoter was marginal, and it was not affected by the ETFDH status in the cell (Fig.5E). Finally, silencing of BCL-6 in NT2197 and 4T1 ETFDH KO cells increased 4E-BP1 protein levels (Fig.5F-G). These results suggested that BCL-6 is in part responsible for the transcriptional repression of *EIF4EBP1*

triggered by ETFDH abrogation. We then assessed whether BCL-6 is implicated in the effects of ETFDH loss on proliferation. These experiments revealed that depletion of BCL-6 attenuates proliferation of ETFDH KO 4T1 cells (Fig.5H). Collectively, these data show that BCL-6 is likely to act as a mediator of the effects of ETFDH abrogation on reduction in *EIF4EBP1* expression and increased proliferation of cancer cells.

Reduced *ETFDH* expression affects neoplastic growth in a dosage-dependent manner.

Thus far, we established that ETFDH loss drives neoplastic growth by enticing bioenergetic rewiring, downregulating *EIF4EBP1* expression and inducing mTORC1 signaling. However, ETFDH is not lost, but rather downregulated in human cancers. Indeed, data available in cBioPortal from 2683 samples across cancer types [38] indicate that missense or truncating mutations in ETFDH are rare (0.3%) (Fig.6A). Of note, we observed that DNA methylation inhibitors, 5-azacytidine (5-aza) and 5-aza-2′-deoxycytidine (5-aza-2-deoxyC) increased ETFDH protein levels in HCT-116 cells (Fig.6B), thus suggesting that one of the potential mechanisms of downregulated *ETFDH* expression in neoplasia may stem from increased DNA methylation. Based on these observations, we developed a model that more closely reflects downregulation, but not a complete ETFDH loss in human tumors. To this end, we took advantage of a recently designed method based on targeted poly(A) track insertion within endogenous genes to induce ribosome stalling and frameshifting, resulting in mRNA degradation and reduction in corresponding protein levels [39]. The length of the poly(A) track directly correlates with the reduction in amount of protein produced, allowing for the investigation of gene-dosage effects on ensuing phenotypes [39,40]. Accordingly, mutants were designed by inserting poly(A) tracks of 12 and 18 adenosines [12A, equivalent to 4 consecutive AAA (Lys) codons $(AAA)_4$; 18A, equivalent to 6 consecutive AAA (Lys) codons $(AAA)_6$], as well as control track (CTRL) [6 consecutive lysine AAG codons

$(AAG)_6$] using site-directed mutagenesis (Fig.S6A, see methods). Based on Alphafold rendered structure (version 2)[41,42], we chose residue 38 in an unstructured loop of Etfdh, which was selected as insertion sites for $(AAA)_4$, $(AAA)_6$ or $(AAG)_6$ tracks (Fig.S6B). This strategy was used to minimize inadvertent effects caused by inserting poly Lys stretches into the possible mitochondrial import sequence and globular part of the protein. Of note, $(AAA)_6$ and $(AAG)_6$ stretches are translated in the equal number of Lys residues, whereby (AAA), but not (AAG), stretches cause ribosome stalling and a decrease in corresponding protein levels (Fig.6C). To this end, the construct harboring $(AAG)_6$ was used as a control to further mitigate potential inadvertent effects of insertion of poly-Lys on the function of the protein. We then expressed $(AAG)_6$, $(AAA)_4$, or $(AAA)_6$ *Etfdh* constructs in ETFDH KO NT2197 cells. As previously reported [39], insertion of $(AAA)_4$ and $(AAA)_6$ stretches progressively reduced ETFDH protein abundance as compared to insertion of $(AAG)_6$ track (Fig.6C). The reduction in ETFDH protein levels was mirrored by a gene-dose dependent increase in mTORC1 signaling as monitored by induction of phospho-rpS6 (Ser240/244; Fig.6C). ETFDH gene-dosage dependent increase in BCL-6 and reduction in 4E-BP1 protein abundance were also observed, while dose-dependent decrease in ETFDH protein abundance did not have a major effect on 4E-BP2 protein levels (Fig.6C). Accordingly, *Eif4ebp1* RNA levels were reduced in dose-dependent manner, while *Eif4ebp2* RNA levels were unaffected (Fig.6D). Moreover, reduction in ETFDH protein levels correlated with increased mtDNA content (Fig.6E), oxygen consumption (Fig.6F), ATP production from OXPHOS (JATPox) (Fig. 6G), bioenergetic capacity (Fig.6H), and cell proliferation (Fig.6I). Finally, we compared the growth of tumors formed by ETFDH KO NT2197 cells in which ETFDH expression was rescued by expressing a construct carrying $(AAA)_6$ or a control $(AAG)_6$ track in SCID-BEIGE mice. These experiments revealed that the tumors carrying $(AAA)_6$ insertions exhibit increased tumor growth and larger final tumor volumes relative to control tumors expressing $(AAG)_6$ insertions (Fig.6J-

K). Altogether, these findings demonstrate that ETFDH gene-dosage critically influences cellular bioenergetics, mTORC1 signaling, 4E-BP1 levels, proliferation and tumor growth. Accordingly, ETFDH gene-dosage is likely to influence neoplastic growth and aggressiveness of cancer cells.

Discussion

We uncovered a previously unrecognized role of ETFDH in neoplasia. We show that ETFDH expression is decreased across a broad spectrum of cancers, and that ETFDH downregulation gives a proliferative advantage *in vitro* and accelerates tumor growth *in vivo*. ETFDH mutations play a major role in a group of metabolic disorders collectively referred to as MADD. In contrast, mutations in ETFDH are rare in cancer (Fig.6A), but downregulation of ETFDH levels is common and likely occurs at least in part as a consequence of DNA hypermethylation, an event that is frequently observed among tumor suppressor genes [43]. Mechanistically, we demonstrate that abrogation of the ETFDH gene leads to accumulation of intracellular amino acids, particularly those with branched chains. This in turn triggers mTOR signaling. Aberrant activation of mTOR signaling occurs frequently in neoplasia [44], leading to increased protein synthesis, mitochondrial functions [26,45] and metabolic perturbations [4,46] that fuel cancer growth and dissemination. Surprisingly, in addition to mTOR hyperactivation, we observed a prominent decrease in 4E-BP1 (but not 4E-BP2) mRNA and protein levels upon ETFDH abrogation. The mTORC1/4E-BP axis contributes to metabolic plasticity through translational upregulation of non-essential amino acid biosynthetic enzymes [4], and promotes mitochondrial biogenesis [25] while influencing mitochondrial dynamics [47]. Accordingly, mTORC1 controls cell proliferation through 4E-BPs [23,48].

Importantly, restoration of 4E-BP1 levels largely reverted bioenergetic and pro-neoplastic phenotypes associated with ETFDH loss (Fig.4G-I). This is consistent with previously attributed tumor-suppressive effects of 4E-BP1 effects [49-53]. More recently, it has been demonstrated that

under certain contexts 4E-BPs may play a beneficial role for tumor survival. For instance, 4E-BPs may facilitate tumor growth by regulating global and selective mRNA translation under periods of cellular stress [54,55], including suppression of fatty acid biosynthesis under glucose deprivation [56,57]. Collectively, these findings demonstrate that 4E-BPs are likely to play more complex, context dependent roles during cancer progression than previously anticipated. Moreover, the role of different 4E-BP proteoforms in cancer was in general thought to be redundant. Our findings demonstrate that in the context of ETFDH abrogation selective decrease in 4E-BP1, but not 4E-BP2 levels plays a role in driving neoplastic growth thereby suggesting that 4E-BP1 and 4E-BP2 may play non-overlapping roles at least in a subset of cancers.

Considering that disruption of ETFDH resulted in altered *EIF4EBP1* mRNA levels, but not translation nor mRNA/protein stability, we set out to identify transcription factors that may mediate the effects of ETFDH loss on reduction in 4E-BP1 levels. These experiments highlighted that transcriptional repression of *EIF4EBP1* in ETFDH deficient cells is at least in part mediated by BCL-6, whose expression is increased upon ETFDH abrogation (Fig.5A). Notably, BCL-6 was previously described as an *EIF4EBP1* repressor in skeletal muscle [34]. BCL-6 is overexpressed across various cancer types [58] and is positively regulated by the mTOR [35-37]. BCL-6 allows cells to mitigate several stresses, including genotoxic [32], proteotoxic [58], and oxidative stress [59]. BCL-6 has also been shown to inhibit glycolysis [60] and fatty acid biosynthesis [61], thereby influencing metabolic rewiring. Notably, BCL-6 is associated with increased cell proliferation across cancer types [62]. ETFDH KO cells have increased BCL-6 expression (Fig.5A), while BCL-6 depletion attenuates the hyper-proliferative phenotype of ETFDH KO cells (Fig.5F). Thus, the induction of cell proliferation and adaptation to various stressors in the context of ETFDH reduction appears to be BCL-6 dependent.

It is important to note that although ETFDH expression is downregulated across a broad spectrum of human malignancies, its expression is rarely lost in cancer (Fig.6A). Indeed, ETFDH is found among under-expressed metabolic enzymes in a study that compiled cancer microarray datasets [63].To model reduced ETFDH expression, we performed ETFDH gene-dosage experiments by taking advantage of a recently developed method wherein insertion of poly(A) stretches in coding region of a gene of interest leads to ribosome stalling during elongation and degradation of corresponding mRNA and protein [39]. These experiments demonstrated that ETFDH regulates cellular bioenergetics, mTORC1 signaling, 4E-BP1 levels, and proliferation in gene-dosage dependent manner, and thus may act as a haploinsufficient tumor suppressor. Nonetheless, we did not observe a major effect of ETFDH disruption on proliferation, mTOR signaling or 4E-BP1 levels in non-transformed murine breast epithelial NMuMG cells. These findings suggest that the decreased expression of ETFDH may not be sufficient for malignant transformation, while playing a major role in tumor maintenance and progression.

Intriguingly, we observed that ETFDH expression is at least in part reduced through DNA methylation. This suggest that epigenetic changes driven by DNA methylation may be one of the factors predicting cancer cell dependence on downregulation of ETFDH while contributing to ETFDH-related phenotypes. Moreover, recent studies highlighted cross-talk between aberrant mTOR signaling and epigenetic perturbations [64-67], which further reinforces the plausibility that epigenetic reprograming in cancer cells may underpin the pro-neoplastic role of ETFDH downregulation and/or explain ensuing phenotypes.

In conclusion, we show that under-expression of ETFDH drives neoplastic growth. These findings depict how disruption of mitochondrial enzyme retrogradely signals to influence oncogenic signaling programs, which orchestrate metabolic changes that engender tumor progression.

Limitations of the Study

Considering that this is a pioneering study in investigating the potential role of ETFDH in cancer, we focused mainly on using tumor growth as the endpoint of the *in vivo* experiments. Future studies are thus warranted to investigate the role of ETFDH in tumor dissemination and metastatic spread. Finally, although we show that the increase in mTOR signaling triggered by ETFDH disruption is at least partially mediated by the accumulation of intracellular amino acids, we did not determine whether these effects are amino acid specific. Considering a well-established mechanisms of amino acid sensing by mTOR, it is likely that these effects are ultimately mediated via Rags [68] or HOPS complex [69].

Resource availability

Lead contact

Further information and requests for reagents may be directed upon reasonable request by the lead contact, Ivan Topisirovic (ivan.topisirovic@mcgill.ca).

Materials Availability

Plasmids generated in this study will be deposited to Addgene.

Data and code availability

The original data will be deposited and available at Mendeley Data. This paper does not report original code.

Acknowledgments

We are thankful to the members of all involved laboratories for helpful discussions. We thank Luc Choinière and Mariana Russo for assistance with metabolomic experiments and Christian Young for assistance with flow cytometry. This research was funded by the Terry Fox Foundation (TFF)

Oncometabolism Team Grant (TFF-242122) to I.T., P.S, and M.P, and Canadian Institutes of Health Research (CIHR) (PJT-183843, PJT-479494) to I.T. Research in OL's lab is supported by grants from the Swedish Research Council (2020-01665), Swedish Cancer Society (22 2186), the Cancer Research Funds of Radiumhemmet (231263) and the Wallenberg Academy Fellow Program. L-M.P. acknowledges the funds from Queen's University. D.P. is supported by CIHR Postdoctoral Fellowship (MFE-171312) and Cancer Research Society (CRS) The Next Generation of Scientists Award (NGS). P.J. and H.K. are supported by Fonds de Recherche du Québec – Santé (FRQS) Fellowships. I.T. is supported by FRQS Senior Investigator award. Metabolic analysis was performed at the Rosalind and Morris Goodman Cancer Research Centre's Metabolomics Core Facility, which is supported by the Canada Foundation for Innovation, the Dr. John R. and Clara M. Fraser Memorial Trust, the Terry Fox Foundation (TFF Oncometabolism Team Grant; TFF-242122), and McGill University.

Author Contributions

Conceptualization, D.P., M.P. and I.T.; Methodology, D.P., R.P., P.J., S.I., H.K., T.B., and S.D.; Formal Analysis, D.P., P.J., S.T., E.C., S.I., K.J.S. and T.B.; Investigation, D.P., R.P., P.J., S.T., E.C., V.S., S.I., S.M., L.Z., H.K., N.C., K.J.S., J.Z., J.V., F.A., and S.M.; Resources, E.G., M.T, D.A., O.L., L.-M.P., S.D., J.U.-S., P.M.S., M.P., and I.T.; Writing – Original Draft, D.P., M.P., and I.T.; Writing – Review & Editing, all authors; Supervision, M.P., and I.T.; Project Administration, M.P., and I.T.; Funding Acquisition, D.P., M.P., and I.T.

Declaration of interests

The authors declare no conflict of interest.

Declaration of generative AI and AI-assisted technologies

AlphaFold Protein Structure Database (Google Deepmind) was used in the preparation of ETFDH poly(A) track mutants. Following the use of this tool, the authors reviewed the content and take full responsibility for the content of the publication.

Figure Legends

Figure 1: ETFDH loss promotes tumor growth

A) ETFDH expression in non-adjacent tissue (NAT) or grade 3 cancerous tissue (Tumor) using IHC on colorectal cancer tissue microarray. Staining intensity of DAB in arbitrary units (A.U) is shown. Data are presented as means +/- SEM (NAT n=14, Tumor n=13), **$p<0.01$, unpaired Student's *t* test.

B-C) Tumor growth of WT EV, ETFDH KO, and ETFDH Rescue HCT-116 cells following intra-caecal injection (B) and endpoint volumes of tumors (C). Growth was assessed by luminescence (photons). Data are presented as means +/- SEM (WT EV n=6, ETFDH KO n=8, ETFDH Rescue n=8), *$p<0.05$, one-way ANOVA, Tukey's post-hoc test.

D-E) Tumor growth of WT and ETFDH KO NT2197 cells following mammary fat-pad injection (D) and endpoint volumes of tumors (E). Growth is assessed using calipers. Data are presented as means +/- SEM (WT n=17, ETFDH KO n=17), *$p<0.05$, unpaired Student's t test.

Related to Figure S1

Figure 2: Absence of ETFDH promotes mitochondrial metabolism

A-B) Oxygen consumption (A) and extracellular acidification (B) for WT EV, ETFDH KO, and ETFDH Rescue HCT-116 cells was determined using a Seahorse bioanalyzer. Data are normalized

to cell count. Data are presented as means +/- SD (n=4), *p<0.05, **p<0.01, one-way ANOVA, Tukey's post-hoc test.

C) Basal *J* ATP calculations from WT EV, ETFDH KO, and ETFDH Rescue HCT-116 cells. *J* ATP ox represents ATP production from oxidative phosphorylation, while *J* ATP glyc is ATP production from glycolysis. Comparison between *J* ATP ox (grey bars; top) and *J* ATP glyc (white bars; bottom) is shown. Data are presented as means +/- SD (n=4), *p<0.05, **p<0.01, one-way ANOVA, Tukey's post-hoc test.

D-E) Bioenergetic Plot for Basal, FCCP, and Monensin *J* ATP fluxes (D) and Bioenergetic Capacity (E) for WT EV, ETFDH KO, and ETFDH Rescue HCT-116 cells. Data are presented as means +/- SD (n=4), *p<0.05, one-way ANOVA, Tukey's post-hoc test.

F) Glutamine uptake and glutamate production from WT and ETFDH KO HCT-116 cells. Results are shown as fold changes of ETFDH KO cells relative to WT cells. Data are presented as means +/- SD (n=3), *p<0.05, paired Student's *t* test.

G) Schematic of ^{13}C-glutamine tracing throughout the citric acid cycle (CAC). Isotopomers labelled in green depict ^{13}C-glutamine tracing in the forward direction of the CAC, while those in purple represent reverse tracing.

H) Relative abundance of ^{13}C-labelled metabolites in the forward (green) and reverse (purple) directions from WT (blue) and ETFDH KO (red) NT2197 cells. Data are presented as means +/- SD (n=3), *p<0.05, **p<0.01, ***p<0.001, ****p<0.0001, paired Student's *t* test.

I) Proliferation of WT and ETFDH KO HCT-116 cells grown in the absence or presence of glutamine for 48 hours. Results are shown as fold changes of counts grown under glutamine deprivation relative to counts grown under glutamine repleted (2mM) conditions. Data are presented as means +/- SD (n=3), *p<0.05, paired Student's *t* test.

Related to Figure S2

Figure 3: ETFDH loss bolsters mTORC1 signaling and downregulates 4E-BP1 protein levels.

A) Amino acid profile in WT and ETFDH KO HCT-116 and NT2197 cells. Data are presented as fold change of ETFDH KO compared to WT (n=3).

B) Puromycin incorporation assays in WT and ETFDH KO HCT-116 cells. Levels and phosphorylation status of indicated proteins were determined via western blotting using indicated antibodies. β-Actin was used as a loading control (representative blots of n=3).

C) Levels and phosphorylation status of indicated proteins in WT or ETFDH KO HCT-116 and NT2197 cells were determined by western blotting. β-Actin served as a loading control (representative blots of n=3).

D) Levels and phosphorylation status of indicated proteins in WT EV, ETFDH KO, or ETFDH Rescue HCT-116 and NT2197 cells were determined by western blotting. β-Actin was used as a loading control (representative blots of n=3).

E) Total and phosphoprotein levels in WT or ETFDH KO HCT-116 cells were determined by western blotting using indicated proteins. Cells were serum starved overnight, then depleted of amino acids for indicated timepoints (0, 10, 30, 60 minutes), or stimulated with FBS for 4 hours (Stim). β-Actin was used as loading control (representative blots of n=3).

F) Quantification of pS6(S240/244)/S6 ratio from data presented in panel E. Quantification of amino acid starved cells (left) or serum stimulated cells (right). Data are presented as means +/- SD (n=3). *Left:* *$p<0.05$, one-way ANOVA, Tukey's post-hoc test. *Right:* paired Student's *t* test.

G) Quantification of p4E-BP1(S65)/4E-BP1 ratio from data presented in panel E. Quantification of amino acid starved cells (left) or serum stimulated cells (right). Data are presented as means +/- SD (n=3). *Left:* *$p<0.05$, one-way ANOVA, Tukey's post-hoc test. *Right:* paired Student's *t* test.

Related to Figure S3

Figure 4: Repression of *EIF4EBP1* transcription mediates the effects of ETFDH loss on cancer bioenergetics and tumor growth

A) Levels and phosphorylation status of indicated proteins in WT EV, ETFDH KO, or ETFDH Rescue HCT-116 and NT2197 cells were determined by western blotting. β-Actin was used as a loading control (representative blots of n=3).

B) Levels of indicated protein in λ-phosphatase treated WT or ETFDH KO HCT-116 and NT2197 cell lysates were monitored by western blotting. β-Actin was used as a loading control (representative blots of n=3).

C) Indicated protein levels in WT or ETFDH KO HCT-116 tumors were determined by western blotting. AKT was used as loading control (WT n=8, ETFDH KO n=11).

D-E) Quantification of 4E-BP1 (D) and 4E-BP2 (E) from tumors described in panel C. Data are presented as means +/- SEM (WT n=8, ETFDH KO n=11), ***$p<0.001$, unpaired Student's *t* test.

F) m^7GDP pulldown assay in ETFDH KO and ETFDH KO overexpressing 4E-BP1 (ETFDH KO 4E-BP1) NT2197 cells. Specified protein levels in m^7GDP pulldown or input were determined by western blot. β-Actin was used as loading control (input) and used to exclude contamination in the pulldown material (m^7GTP bound) (representative blots of n=3).

G) Oxygen consumption of ETFDH KO and ETFDH KO 4E-BP1 NT2197 cells. Data are normalized to cell count and presented as means +/- SD (n=5), **$p<0.01$, Student's *t* test.

H-I) Tumor growth of ETFDH KO and ETFDH KO 4E-BP1 NT2197 cells following mammary fat-pad injection (H) and endpoint volume of tumors (I). Growth was assessed using caliper measurements. ETFDH KO measurements are the same as in Fig.1D. Data are presented as means +/- SEM (ETFDH KO n=17, ETFDH KO 4E-BP1 n=18), **$p<0.01$, unpaired Student's *t* test.

J) Mitochondrial DNA in WT EV, ETFDH KO, and ETFDH Rescue HCT-116 cells was quantified by qPCR. Mitochondrial DNA (mtDNA) content is normalized to genomic DNA (gDNA) content.

Data are presented as fold change relative to WT EV cells +/- SD (n=3), *p<0.05, **p<0.01, one-way ANOVA, Tukey's post-hoc test.

K) Levels of indicated proteins in WT EV, ETFDH KO, and ETFDH Rescue HCT-116 cells were assessed by western blotting. β-Actin was used as a loading control (representative blots of n=3).

L) *EIF4EBP1* and *EIF4EBP2* mRNA levels in WT EV, ETFDH KO, and ETFDH Rescue HCT-116 cells were determined by RT-qPCR. *PP1A* was used as a house-keeping gene. Data are presented as fold change relative to WT EV cells +/- SD (n=3), *p<0.05, one-way ANOVA, Tukey's post-hoc test.

M) *Eif4ebp1* and *Eif4ebp2* mRNA abundance in WT and ETFDH NT2197 KO cells was determined by RT-qPCR. *Actb* was used as a house-keeping gene. Data are presented as fold change relative to WT cells +/- SD (n=3), *p<0.05, paired Student's *t* test.

Related to Figure S4

Figure 5: Loss of ETFDH increases BCL-6 levels leading to BCL-6-dependent inhibition of *EIF4EBP1* transcription.

A) Levels of indicated proteins in WT or ETFDH KO HCT-116 and NT2197 cells were determined by western blotting. β-Actin was used as a loading control (representative blots of n=3).

B) *BCL6/Bcl6* mRNA abundance in WT and ETFDH KO HCT-116 and NT2197 cells was determined by RT-qPCR. *PP1A* mRNA was used as a control for HCT-116 experiments, while *Actb* mRNA was used as a control for NT2197 experiments. Data are presented as fold change relative to WT cells +/- SD (n=3), paired Student's *t* test.

C) Levels of indicated proteins in ETFDH KO NT2197 cells treated with DMSO or Torin1 (250nM) for 4 hours were determined by western blotting. β-Actin was used as a loading control (representative blots of n=3).

D-E) Binding events of BCL-6 to the promoters of *EIF4EBP1* and *EIF4EBP2* were determined by ChIP-qPCR. IgG was used a negative control. Data are presented as % of input (n=3), *p<0.05, two-way ANOVA, Dunnett's post-hoc test.

F) The levels of indicated proteins in ETFDH KO NT2197 cells transfected with siRNA targeting BCL-6 (siBCL-6) or control, scrambled siRNA (siCTRL) were determined by western blotting. β-Actin was used as loading control (representative blots of n=2).

G) Levels of indicated proteins in ETFDH KO 4T1 cells infected with shRNAs targeting BCL-6 (shBCL-6 #1 or shBCL-6#2) or control, scrambled shRNA (shCTRL) were monitored by western blotting. β-Actin served as loading control (representative blots of n=3).

H) Proliferation of ETFDH KO shCTRL, shBCL-6 #1, or shBCL-6#2 4T1 cells. Data are presented as cell count means (n=3), *p<0.05, one-way ANOVA, Dunnett's post-hoc test.

Related to Figure S5

Figure 6: Reduced expression of ETFDH increases mitochondrial metabolism and tumor growth

A) ETFDH mutations from 2683 samples across multiple cancer types. Number of missense and truncating mutations are shown relative to samples with no mutations. Data are acquired from the ICGC/TCGA Pan-Cancer Analysis of Whole Genomes Consortium [38], accessed from the cBioPortal server (www.cbioportal.org)[70-72].

B) Levels of indicated proteins in WT HCT-116 cells treated with 2.5μM 5-azacytidine (5-aza), 10μM 5-aza-2' -deoxycytidine (5-aza-2-deoxyC), or a vehicle (DMSO) for 72 hours were determined by western blotting. β-Actin was used as a loading control (representative blots of n=3).

C) Levels and the phosphorylation status of indicated proteins in ETFDH KO NT2197 cells expressing ETFDH harboring $(AAG)_6$, $(AAA)_4$, $(AAA)_6$ tracks were determined by western blotting. β-Actin was used as a loading control (representative blots of n=3).

D) *Eif4ebp1* and *Eif4ebp2* mRNA abundance in $(AAG)_6$, $(AAA)_4$, and $(AAA)_6$ NT2197 cells were determined by RT-qPCR. *Actb* was used as a house-keeping gene. Data are presented as fold change relative to $(AAG)_6$ NT2197 cells (n=3), *p<0.05, **p<0.01, one-way ANOVA, Dunnett's post-hoc test.

E) Mitochondrial DNA content in $(AAG)_6$, $(AAA)_4$, and $(AAA)_6$ NT2197 cells were monitored by qPCR. Mitochondrial DNA (mtDNA) content was normalized to genomic DNA (gDNA) content. Data are presented as mean fold change relative to $(AAG)_6$ NT2197 cells -/+ SD (n=3), *p<0.05, **p<0.01, one-way ANOVA, Dunnett's post-hoc test.

F) Oxygen consumption of $(AAG)_6$, $(AAA)_4$, and $(AAA)_6$ NT2197 cells was determined using Seahorse bioanalyzer. Data are normalized to cell count and presented as means +/- SD (n=4), one-way ANOVA, Dunnett's post-hoc test.

G-H) Bioenergetic Plot for Basal, FCCP, and Monensin *J* ATP fluxes (G) and Bioenergetic Capacity (H) derived from $(AAG)_6$, $(AAA)_4$, and $(AAA)_6$ NT2197 cells. Data are presented as means +/- SD (n=4), one-way ANOVA, Dunnett's post-hoc test.

I) Proliferation of $(AAG)_6$, $(AAA)_4$, and $(AAA)_6$ NT2197 cells. Data are presented as cell count means +/- SD (n=4), **p<0.01, one-way ANOVA, Dunnett's post-hoc test.

J-K) Tumor growth of $(AAG)_6$ and $(AAA)_6$ NT2197 cells following mammary fat-pad injection (J) and endpoint volumes of tumors (K). Growth was assessed using calipers. Data are presented as means +/- SEM ($(AAG)_6$ n=6-12, $(AAA)_6$ n=11-13), **p<0.01, unpaired Student's *t* test.

Figure 7: ETFDH reduction enhances tumor growth

Schematic representation of the model whereby reduction in ETFDH levels accelerates tumor growth. Reduction of ETFDH triggers accumulation of intracellular amino acids thus increasing mTORC1 signaling. This is orchestrated with BCL-6-dependent reduction in 4E-BP1 levels to drive mitochondrial biogenesis and increase bioenergetic capacity of cancer cells ultimately leading to more aggressive tumor growth.

Related to Figure S6

STAR★Methods

Experimental model and study participant details

Cell lines and cell culture

HCT-116, NALM6, and HEK293T cells were obtained from American Type Culture Collection (ATCC) and verified using ATCC Cell line authentication service. NMuMG, NT2197, and MT4788 Parental and STAT1 KO cells were obtained by Dr. J. Ursini-Siegel's lab, while 4T1 (4T1-526) cells were obtained from Dr. P.M. Siegel's group. HEK293T and HCT-116 cells were cultured in DMEM supplemented with 10% fetal bovine serum (FBS), 1% penicillin/streptomycin and supplemented with 2mM L-Glutamine to obtain a final concentration of 6mM L-Glutamine. 4T1 and NALM6 cells were cultured in RPMI-1640 supplemented with 10% FBS, 1% penicillin/streptomycin and 2mM L-Glutamine as previously described [73]. NMuMG and NT2197 cells were cultured in DMEM supplemented with 10% FBS, 1% penicillin/streptomycin, 2mM L-Glutamine, 10 mg/mL insulin, 20 mM HEPES, pH 7.5. NT2197 culture media was supplemented with puromycin (2 μg/mL) as previously described [15]. MT4788 were grown in DMEM, 2.5% FBS, mammary epithelial growth supplement (MEGS), 1% penicillin/streptomycin and gentamycin as

previously described [29]. All cell lines were maintained at 37°C and 5% CO2 in a humidified environment and tested periodically for mycoplasma according to the manufacturer's instructions.

Animals

6–8-week-old SCID-BEIGE mice were purchased from Charles River. Male SCID-BEIGE mice were used for intracaecal experiments, while female mice were used for mammary fat pad injections. All animal experiments were performed in accordance with the guidelines of the McGill University Animal Ethics Committee and the Canadian Council on Animal Care as approved by the facility animal care committee.

Method details

Generation of ETFDH Knockout Cell Lines

To deplete endogenous ETFDH expression in HCT-116 and NALM6 cells, two guides RNA (gRNAs) targeting exon 6 and exon 9 of human ETFDH (against ETFDH sequences AGGTTGGCCGAATGCTAGGATGG and GATGTAGGGATACAAAAGGATGG) (refer to Key Resource Table for gRNA sequences) were designed using CHOPCHOP (https://chopchop.cbu.uib.no/)[74] and purchased with the appropriate overhangs to be cloned into LentiCRISPRv2(GFP) (Addgene #82416). Cloning was carried out as previously described [75,76], with the following modifications: BsmBI-v2 (New England Biolabs) was used to digest the lentiCRISPRv2 plasmid; plasmid DNA was recovered using Zymoclean Gel DNA Recovery Kit (Zymo Research), and ligation was performed overnight at 4°C. Transformation of the ligated plasmid was carried out at 42°C in chemically competent Stbl3 cells (Fisher Scientific). Bacteria were plated on Lysogeny Broth (LB)-agar plates containing ampicillin (1 µg/mL) (BioBasic). Extraction of plasmid DNA was conducted using the QIAprep Spin Miniprep Kit (Qiagen) and samples were sequenced using primer for human U6 promoter (refer to Key Resource Table for

sequence). Nucleofection was used to deliver the validated lentiCRISPRv2 plasmids into HCT-116 and NALM6 cells. Transfections of the plasmids were carried out in Nucleofector cuvettes, according to the optimized protocols for NALM6 and HCT-116 cells (Lonza Bioscience), with 1×10^6 cells used and 1X PBS was used instead of the commercial 4-D Nucleofector solution. Post-nucleofection, cells were allowed to grow for 72 hours at 37°C, 5% CO_2, prior to cell sorting (BD FACSAria™ Fusion Flow Cytometer (BD Biosciences)). Cells expressing GFP were selected and grown in 96-well plates containing conditioned media (45% filtered culture media, 45% fresh media, & 10% FBS). After two weeks, sorted clones were transferred into 24-well plates and later into 6-well plates to be collected and validated. Depletion of endogenous ETFDH protein levels in both HCT-116 and NALM-6 cells was initially confirmed by immunoblotting. Candidate clones with loss of ETFDH expression were kept for further validation. Moreover, the genomic DNA loci of candidate clones were sequenced and analyzed for insertion–deletion mutations (INDELs). Two sets of PCR primers were designed in regions flanking the CRISPR target sites (refer to Key Resource Table for validation PCR sequences). Extraction of genomic DNA for each clone was carried out using the PureLink Genomic DNA Mini Kit (Fisher Scientific). Two rounds of polymerase chain reaction (PCR) on the extracted genomic DNA (35 PCR cycles with Set 1 followed by 45 PCR cycles with Set 2) were carried out and gel electrophoresis was utilized to separate the PCR products. The smaller PCR product for each clone was excised and purified using the Zymoclean Gel DNA Recovery Kit (Zymo Research). The products were sequenced, and chromatograms were analyzed for the presence of mutations causing a premature stop-codon or a frameshift. Insertion–deletion mutations (INDELs) in *ETFDH* were verified by PCR followed by sequencing, while the absence of ETFDH protein was confirmed by western blotting for HCT-116 cells (Fig.S1G) and NALM6 cells (Fig.S1J).

To deplete ETFDH expression in NMuMG, NT2197 and 4T1 cells, two guides (gRNAs) targeting exon 2 of mouse Etfdh (against mEtfdh sequences 5'-ATTTTTATGCAGCGTATCACTGG-3' and 5'-GAACATCTTGGAGCACACAGAGG-3') were designed using CHOPCHOP and cloned in LentiCRISPRv2(GFP) (Addgene #82416) and sequenced as shown above. For lentiviral production, 2.5×10^5 HEK293T cells were seeded overnight in a 6-cm dish (Sarstedt). The next day, cells were co-transfected with 4µg of respective lentiCRISPRV2 GFP plasmid containing either one of the gRNA inserts or empty-lentiCRISPRV2 GFP plasmid, 2.66µg of psPAX2 packaging plasmid (Addgene 35002), and 1.66 µg of pMD2.G plasmid (Addgene #12259) using the jetPRIME transfection reagent as described by the manufacturer's protocol (Polyplus transfection). Growth media was changed after 24 hours. After 48 hours, viral supernatant was filtered (0.45 µm filter; (Frogga Bio)), mixed 1:1 with fresh culture media, and applied to target cells grown in 6-well plates along with 8 µg/mL polybrene (Sigma-Aldrich). Cells were re-transduced the following two days with viral supernatant. Cells were allowed to recover for 48 hours post-transduction. Cells were sorted into 96-well plates (Sarstedt) and grown to generate stable cell lines, as shown above. Depletion of mouse Etfdh protein levels was initially confirmed via immunoblotting for NT2197 (Fig.S1H), 4T1 (Fig.S1I), and NMuMG (Fig.S1K). The presence of INDELs leading to a premature stop codon or frameshift was determined by sequencing as shown above. Two sets of PCR primers were designed in the regions flanking the CRISPR target sites (refer to Key Resource Table for validation PCR sequences).

Generation of ETFDH Rescue Cell Lines

To rescue human ETFDH expression in HCT-116 cells, ETFDH(NM_004453) Human Tagged ORF was cloned into pLenti-ETFDH-C-Myc-DDK-P2A-Puro plasmid according to the manufacturer's instructions (Origene). The resulting plasmid, pLenti-ETFDH-C-Myc-DDK-P2A-Puro, was transfected with psPAX2, pMD2.G into HEK293T cells with JetPrime reagent

(Polyplus) according to the manufacturer's instructions. Viral supernatants were filtered (0.45µM) and applied to HCT-116 ETFDH KO cells with polybrene (6µg/mL). After 6 hours, cells were re-infected overnight. After 2 days, selection with puromycin (4µg/ml) was performed for 72 hours. Uninfected cells were selected with puromycin to serve as negative controls. The re-introduction of ETFDH expression or control plasmid in the knockout cells was confirmed via western blotting (Fig.S1G).

To rescue ETFDH expression in NT2197 ETFDH KO cells, a lentiviral plasmid conferring hygromycin B resistance and expressing mEtfdh with PAM site mutations or expressing an ORF-Stuffer was created using VectorBuilder (VB221206-1257xet and VB900123-2599cba respectively). Lentivirus production and transduction were carried out as previously mentioned for three consecutive days. After 48h of recovery, cells were selected with 1 mg/mL hygromycin B for 3 days. Cells were confirmed by western blotting (Fig.S1H).

Generation of Poly(A) Track ETFDH Variants

Mutants were designed by inserting poly(A) tracks of multiple adenosines: control track (CTRL) [6 consecutive lysine AAG codons $(AAG)_6$], 12 adenosines [12A, equivalent to 4 consecutive AAA (Lys) codons $(AAA)_4$; 18 adenosines [18A, equivalent to 6 consecutive AAA (Lys) codons $(AAA)_6$] within the rescue plasmid pLV[Exp]-Hygro-EF1A>mEtfdh (Fig.S6A). The polyA track insertion site was determined using AlphaFold (version 2)[41,42] to minimize unintended effects caused by the poly-lysine stretches on the possible mitochondrial import sequence. The polyA tracks were inserted following residue 38, in an unstructured loop of the Etfdh protein (Fig.S6B). Site-directed mutagenesis was performed using QuikChange II site-directed mutagenesis kit, according to the manufacturer's instructions (Agilent). Briefly, cycling parameters are followed as: Cycle 1: 95°C for 1min; Cycle 2: 95°C for 30 sec, 60°C for 30 sec, 68°C for 10min; Cycle 3: 68°C for 7min. The resulting plasmids were generated: pLV[Exp]-Hygro-EF1A>mEtfdh-AAG_6,

pLV[Exp]-Hygro-EF1A>mEtfdh-AAA_4, pLV[Exp]-Hygro-EF1A>mEtfdh-AAA_6. To generate the poly(A) track Etfdh mutant lines in NT2197 cells (termed AAG_6, AAA_4, AAA_6), lentivirus production and transduction into NT2197 ETFDH KO cells was carried out as previously mentioned for three consecutive days. After 48h of recovery, cells were selected with 1 mg/mL hygromycin B for 3-4 days. ETFDH expression was confirmed by western blotting (Fig.6C).

Generation of Cells Expressing *EIF4EBP1*

pBABE-puro-EV and pBABE-puro-4E-BP1 plasmids were used to overexpress 4E-BP1 in HCT-116 ETFDH KO cells. Retrovirus production and transduction was carried out similarly to lentivirus production, except 2.66 µg of pUMVC packaging plasmid (Addgene #8449) was utilized instead of psPAX2. Following three consecutive days of viral transduction, cells were allowed to recover for 48h prior to selection with 2 µg/mL puromycin (Sigma-Aldrich) for 3 days. To overexpress 4e-bp1 in NT2197 ETFDH KO cells, plasmids containing m4e-bp1 or ORF-Stuffer were generated by VectorBuilder (VB221206-1246sbx & VB900123-2599cba). Lentivirus production and transduction was carried out as previously mentioned for three consecutive days prior to a 48h recovery period. After this period, selection with hygromycin B (1 mg/mL) was conducted for 5-7 days. Validation was observed by western blotting (Fig.4F).

Generation of Knockdown Models by shRNA/siRNA

Knockdown using shRNA was performed as previously described [4]. Briefly, HEK293T cells were transfected with psPAX2, pMD2.G or target pLKO.1 lentiviral shRNA vectors with JetPrime reagent (Polyplus) according to the manufacturer's instructions. Viral supernatants were filtered (0.45µM) and transferred to target cells with polybrene (6µg/mL). After 6 hours, cells were re-infected overnight. After 2 days, selection with puromycin (4µg/ml) was performed for 72 hours. Uninfected cells were selected with puromycin to serve as negative controls. Cells were seeded

and processed for protein extraction or cell proliferation. Validation was confirmed by western blotting for *BCL6* knockdown (Fig.5E) and *RAPTOR* or *RICTOR* knockdown (Fig.S3E).

Knockdown using siRNA was performed as previously described [77]. Briefly, target cells were transfected for 24 hours with 50nM Silencer Negative Control No.1 (Thermofisher) or BCL6 siRNA (Thermofisher) using JetPrime reagent (Polyplus) according to the manufacturer's instructions. Cells were re-transfected the next day for 24 hours, then processed for protein extraction. Validation was confirmed by western blotting (Fig.5D).

Cell Proliferation Assay

Cells were counted using a Countess automated cell counter (Invitrogen) and trypan blue exclusion was used for determining cell viability. Cells (HCT-116, NT2197, NMuMG, 4T1, NALM-6, and MT4788) were seeded in 6-well dishes and counted to 3-5 days. For glutamine deprivation experiments, HCT-116 cells were seeded in full culture for 24 hours. The next day, cells were grown in media in the presence or absence of glutamine for 48 hours and then counted. For Torin1/BiS-35x treatment experiments, HCT-116 cells were seeded overnight. The next day, media was replaced with treatment media containing Torin1 (50nM, 100nM, 250nM, 500nM) or BiS-35X (1nM, 10nM, 100nM, 1000nM) or DMSO for 72 hours and then counted.

Xenograft Experiments

Luciferase-expressing HCT-116 cells (250,000 cells) were injected intracaecally in male (8-10 weeks old) SCID-BEIGE mice as previously described [78]. Tumor growth was monitored and assessed by luminescence (IVIS spectrum, PerkinElmer). Animals were sacrificed after 50 days. Quantification of signal intensity was performed with Living Image software (PerkinElmer). NT2197 mammary tumor cells (50,000 cells) were injected in mammary fat pads of 6-8-week female SCID-BEIGE mice. Tumor growth was monitored using calipers. Measurements were shown as once tumor volume reached 100~200 mm^3 and animals were sacrificed before tumors

reached 1cm^3. Tumors were excised, placed in 10% formalin, and embedded for immunohistochemistry.

Immunohistochemistry

Immunohistochemical staining of colon human parafilm-embedded tissue array (CO992b) was performed as previously described [79]. Briefly, the tissue slide was baked for 55°C for 30 min followed by incubation in xylene (2× 5 min), 100% ethanol (2× 5 min), 95% ethanol (2× 5 min), 75% ethanol (1× 5min), and ddH_2O (2x 5min). The slide was submerged in 10mM sodium citrate buffer (pH 6.0), 0.05% Tween-20 and heat-induced epitope retrieval was carried out in a pressure cooker for 30 min. The slide was cooled for 20 min at room temperature, rinsed in ddH_2O for 5 min, and washed with 1xTBS + 0.3% Triton X-100 for 10 min, then 1xTBS for 5 min at room temperature. The slide was incubated in 3% H_2O_2 for 10 min at room temperature and washed with TBST (1xTBS + 0.1% Tween-20) for 5 min to inactivate peroxidases. A liquid blocker pen (PAP Pen, DAKO) was used to circle tissues on the slide. The TMA was blocked for 1 hour in room temperature in the presence of DAKO Protein Block-Serum Free (DAKO, Cat#X0909). The slide was incubated overnight at 4°C with the ETFDH antibody (1:500, ProteinTech 11109-1-AP). The next day, the slide was washed in TBST (3x 5min), and secondary incubation was performed for 30 min at room temperature with secondary antibody (Antibody background reducing diluent and HRP rabbit substrate (Cell Signaling, Cat#7074)). The slide was washed in TBST (3x 5min) and DAB (Di-amine-benzidine) peroxidase substrate (Vector, Cat# SK-4100) was applied to the slide for 5 min. Reaction was stopped by washing in ddH_2O for 5 min. The slide was counterstained with filtered hematoxylin for 20 sec and rinsed with ddH_2O for 5 min. The slide was placed in 75% ethanol (1 min), 95% ethanol (1 min), 100% ethanol (1 min) and xylene (2x 5min). The slide was mounted with a cytoseal at 60°C and dried in a fumehood overnight. Quantitation of sections was performed using Imagescope software (Aperio).

Western Blotting

Western blotting was performed as previously described[67]. Briefly, cells were washed twice with PBS and lysed with RIPA buffer (50mM Tris-HCl pH 7.5, 150mM NaCl, 0.5% sodium deoxycholate, 1mM PMSF, 1mM DTT, 1% NP40, 0.1% SDS), supplemented with 1X protease inhibitor (Roche) and 1x PhoSTOP (Roche). Lysates were cleared at 4℃ (10min, 13,000rpm). Protein concentrations were determined using BCA kit (ThermoFisher). Lysates were mixed with 5x Laemmli buffer(60mM Tris-HCl (pH 6.8), 10% glycerol, 2% SDS, 5% 2-mercaptoethanol, 0.05% bromophenol blue) and boiled (95℃ for 5min). Proteins were resolved by SDS-PAGE (Bio-Rad) and transferred via wet transfer apparatus (Bio-Rad) to nitrocellulose membranes (Amersham). Membranes were blocked in 5% skim milk (dissolved in TBST (0.1% Tween 20 in 1×TBS)) and incubated in primary antibodies overnight at 4℃. The next day, membranes were washed in TBST and incubated with HRP-conjugated secondary antibodies for 1 hour. Membranes were washed and applied with ECL (Bio-Rad) for 1min. Exposure was carried out on Azure c300 (Azure Biosystems). Images were quantified by ImageJ and analysed using GraphPad Prism10. The list of primary antibodies is described in the Key Resource Table.

For λ-phosphatase experiments, cells were lysed with RIPA and supplemented with 1X protease inhibitor, without 1x PhoSTOP. Protein samples were combined with NEBuffer for protein metallophosphatases (PMP), $MnCl_2$, and λ-protein phosphatase for 30min at 30℃ according to the manufacturer's instructions (New England Biolabs).

Cap-Binding Pull-Down Assay

Assay was carried out as previously described[23]. Briefly, NT2197 cells were seeded overnight in 150mm plates. The next day, media was changed, and cells were washed with PBS and dissolved in lysis buffer containing 50mM MOPS/KOH (7.4), 100mM NaCl, 50mM NaF, 2mM EDTA, 2mM EGTA, 1% NP40, 1% sodium deoxycholate, 7mM β-mercaptoethanol, supplemented with

1X protease inhibitor (Roche) and 1x PhoSTOP (Roche). Lysates were cleared at 4°C (10min, 16,000g). Protein concentrations in samples were elucidated by BCA (ThermoFisher). Samples were equilibrated for 20 min rotating at 4°C with m^7-GDP-agarose beads (Jena Bioscience), then washed in buffer containing 50mM MOPS/KOH (7.4), 100mM NaCl, 50 mM NaF, 0.5mM EDTA, 0.5 mM EGTA, 7 mM β-mercaptoethanol, 0.5 mM PMSF, 1mM Na_3VO_4 and 0.1mM GTP, by centrifugation (500g for 1min). Bound proteins were eluted from beads via boiling in loading buffer. Western blotting was performed on eluted proteins and input samples to assess for eIF4F complex formation using 4E-BP1, eIF4G1, eIF4E, and β-actin antibodies.

Flow Cytometry

NT2197 cells were seeded in 6-well dishes for 24 hours. The next day, cells were stained with 50nM MitoTracker Deep Red (ThermoFisher) for 15 minutes at 37°C in the dark. Cells were washed, counted, and 100,000 cells were dissolved in 500µl HBSS (Gibco). Samples were analyzed with the LSR Fortessa cytometer (Becton Dickinson, Mountain View, CA). Fluorescence intensity was detected by excitation at 644nm and acquisition on the 665/-A channel for MitoTracker Deep Red. ROS measurements were performed as previously described [79]. Briefly, cells were incubated with H_2DCFDA (Molecular Probes) for 30 minutes at 37°C. Cells were trypsinized, washed, and resuspended in 500µl HBSS. Samples were sorted on a BD FACS Canto II system. Fluorescence intensities were calculated by FlowJo (Tree Star, Inc.).

Mitochondrial DNA Quantitation

Quantitation of mitochondrial DNA was carried out as previously described [25]. HCT-116 or NT2197 cells were seeded in 6-well dishes for 24 hours. Genomic and mitochondrial DNA were extracted using PureLink Genomic DNA Mini Kit (ThermoFisher) and quantified by qPCR using

SensiFAST™ SYBR® Lo-ROX kit (Bioline). Primers specific to genomic and mitochondrial DNA are provided in Key Resource Table.

Polysome-Profiling Assay

Experiments were carried out as previously described [80]. Briefly, HCT-116 cells were seeded overnight in 150mm plates. The next day, cells were washed in PBS containing 100 μg/ml cycloheximide and lysed in hypotonic buffer (5 mM Tris-HCl [pH 7.5], 2.5 mM $MgCl_2$, 1.5 mM KCl, 100 μg/ml cycloheximide, 2 mM DTT, 0.5% Triton X-100, and 0.5% sodium deoxycholate). Samples were loaded onto 10%-50% wt/vol sucrose density gradients (20 mM HEPES-KOH pH 7.6, 100 mM KCl, 5 mM $MgCl_2$) and spun on a SW40Ti rotor (Beckman Coulter) at 4°C (36,000 rpm for 2 hours). Samples were fractionated and recorded at OD 254nm using an ISCO fractionator (Teledyne ISCO). RNA from fractions and input was extracted using TRIzol (ThermoFisher) according to the manufacturer's instructions. RNA from each fraction and input was isolated using TRIzol (Invitrogen) according to the manufacturer's instructions. RT-qPCR was performed on fractions and input RNA (refer to section "RNA extraction and RT-qPCR" for more information). Primers are listed in Key Resource Table.

Puromycilation Assay

HCT-116 cells were grown in 10cm dishes for 24 hours. The next day, cells were treated with puromycin (10ug/ml) for 20 minutes. Cells treated with DMSO were used as negative controls. Cells were lysed and protein samples were quantified. Western blotting was performed (refer to "Western Blotting" section for more information) and membranes were incubated in anti-puromycin antibody (Millipore, Cat#MABE343). Quantification of bands was performed by ImageJ.

Stable Isotope Tracing

GC/MS quantification and stable isotope tracing analysis (SITA) was performed as previously described [77]. Briefly, cells were seeded in 6-well dishes. Prior to ^{13}C-glutamine SITA experiments, culture media was replaced with one whose composition contains 2mM unlabelled glutamine for 2 hours. Afterwards, media was replaced with media containing 2mM labelled ([U-13C])-glutamine media (Cambridge Isotope Laboratories, MA, USA; CLM-1822; L-glutamine ([U-13C5]), 99%) for 5, 15, 30, and 60 minutes. For ^{13}C-leucine SITA experiments, culture media was replaced with one containing unlabelled leucine (0.105g/L) for 2 hours, then incubated in media containing labelled (0.105g/L) ([U-13C])-leucine media (Cambridge Isotope Laboratories, MA, USA; CLM-2262-H-0.1; L-leucine ([U-13C6]), 99%) for 24 hours. Both steady state and tracing samples were washed in cold saline solution (9g/L NaCl) and scraped off with 80% methanol. Samples were sonicated at 4°C for 10 minutes (high setting, 30 seconds on/30 seconds off cycles) to rupture cells. Lysates were centrifuged at 4°C (14000g,10 minutes), and supernatants were collected with addition of an internal standard (750ng myristic acid-D27). Samples were dried overnight at 4°C by speed-vac (Labconco). Dried pellets are resuspended in methoxyamine hydrochloride (10mg/ml), sonicated, and cleared for 10 minutes. Samples are heated 70°C for 30 minutes then applied with N-tert-butyldimethylsilyl-N- methyltrifluoroacetamide (MTBSTFA) at 70°C for 1 hour. Derivatized samples are injected into an Agilent 5975C GC/MS (Agilent Technologies, CA, USA) using methods described previously [77]. ^{13}C-tracer samples were run in parallel with unlabelled samples. MassHunter software (Agilent) was used to carry out mass isotopomer distribution analyses, with metabolites normalized to myristic acid-D27 and cell number. Isotopic distributions were corrected for naturally occurring isotopes using an in-house algorithm [81].

RNA Extraction and RT-qPCR

HCT-116 and NT2197 cells were plated in 6-well dishes and extracted using TRIzol (Ambion) or Aurum Total RNA Mini Kit (Bio-Rad) following the manufacturers' instructions. cDNA was synthesized from purified RNA using SensiFAST cDNA Synthesis Kit (Bioline), as per manufacturer's protocol. RT-qPCR was performed using SensiFAST SYBR Lo-ROX kit (Bioline) using methods as previously described [67]. Primers are found in Key Resource Table.

Chromatin Immunopreciptation (ChIP)

Experiments were performed as previously described [67]. Briefly, HCT-116 cells were grown in 150mm dishes and fixed in 4% formaldehyde for 10 min, followed by centrifugation. Pellets were resuspended in ChIP-buffer (50 nM Tris (pH 8), 100 mM NaCl, 5 mM EDTA, 1X PMSF, 2 mM NaF, 0.25% NP-40, 0.25% Triton X-100, 0.25% Sodium Deoxycholate, 0.005% SDS) supplemented with 1x cOmplete protease inhibitor (Roche). Samples are sonicated using Sonic Dismembrator Model 500 (ThermoFisher) at 5 cycles at 20% power, 5 cycles at 25% power, 5 cycles at 30% power; each cycle is 10 sec. Lysates are spun at 4°C (14,000rpm, 10min) and protein concentration was measured from supernatants using the BCA kit (ThermoFisher). Samples were loaded onto Protein G Plus-Agarose Suspension Beads (Millipore) and pre-cleared at 4°C for 3 hours. Input samples were collected, and immunoprecipitation was performed with anti-BCL6 (Cell Signaling, #5650) or anti-IgG (Cell Signaling, #2729) on the remainder of the sample overnight at 4°C. The following day, samples were washed in three wash buffers (20 mM Tris (pH 8), 2 mM EDTA, 0.10% SDS, 1% Triton X-100 with 150/200/599mM for Wash1/2/3 buffers respectively), then a wash with LiCl buffer (10 mM Tris (pH 8), 1 mM EDTA, 0.25 M LiCl, 1% NP-40, 1% Sodium Deoxycholate), and two washes with TE buffer (10 mM Tris (pH 8), 1 mM EDTA). Samples were eluted in elution buffer (0.1 M NaHCO3, 1% SDS), and de-crossliked at 65°C overnight. The following day, proteinase K was applied to samples and heated at 42°C for 1

hour. DNA was purified and collected using DNA collection column (BioBasic). RT-qPCR was performed for *EIF4EBP1* and *EIF4EBP2* using primers found in Key Resource Table.

Respirometry Assay

Oxygen consumption (OCR) and extracellular acidification rate (ECAR) were measured using Seahorse XFe24 and XFe96 analyzers (Agilent) with the Mito Stress Test (Agilent) and Palmitate Oxidation Assay (Agilent), according to the manufacturer's instructions. Briefly, HCT-116 and NT2197 cells were seeded in Seahorse culture plates (XFe24: 50,000 cells or XFe96: 20,000 cells) and incubated at 37°C. Cells were washed twice and incubated in assay media. For mito stress test experiments, assay media is composed of 10mM glucose, 2mM glutamine, and 1mM sodium pyruvate. Injections include oligomycin (1µM), FCCP (1µM), rotenone/antimycin A (1µM), and monensin (20µM). ATP production from OXPHOS (ATPox) or glycolysis (ATPglyc) were quantified using algorithms presented previously [82]. For palmitate oxidation assay, cells were seeded in substrate-limited media (DMEM, 1% FBS, 0.5mM glucose, 1mM glutamine, 0.5mM carnitine). The next day, cells are washed with FAO Buffer (includes 0.5mM glucose, 0.5mM carnitine, and 5mM HEPES). Immediately prior to run, palmitate-BSA or BSA control is added to the cell media. Basal respiration was recorded. Values were normalized to cell counts.

Soft Agar/Colony Formation Assay

Experiments were conducted as previously shown [16]. Briefly, 6-well dishes are filled with a bottom layer solution (1:1; 1% noble agar and 2X culture media (2X DMEM, 20% FBS, 2% Pen/Strep/Glutamine)) per well. Dishes are incubated at room temperature for 30 min to allow solution to solidify. 5,000-10,000 HCT-116 and NT2197 cells are mixed 1:1 with 0.6% noble agar and 2X culture media. 1.5ml of this mixture is transferred on top of the solidified agar wells. Dishes are incubated at room temperature to allow the top layer to solidify. Cells are grown at 37°C until

colony formation is present. Dishes were stained with nitroblue tetrazolium (Sigma), and colonies were counted.

Protein Stability Assay

HCT-116 cells were seeded in 10cm dishes. The next day, cells were treated with cycloheximide (CHX) (50µg/ml) or DMSO for 2 hours. Furthermore, cells were treated with the proteasomal inhibitor, MG-132 (10µM) or DMSO for 2 hours. Final time point for all conditions was 4 hours. Protein was extracted, quantified, and western blotting was performed for ETFDH, p21, 4E-BP1, or β-actin (refer to "Western Blotting" section for more information).

RNA Stability Assay

Assay was performed as previously described [83]. Briefly, HCT-116 cells were seeded in 6-well dishes. The next day, cells were treated with actinomycinD (ActD) for 2,4,8 and 24 hours. RNA was extracted, cDNA was synthesized, and RT-qPCR was performed (refer to "RNA extraction and RT-qPCR" for more information).

Expression Profiles from TCGA/GTEx Databases

Expression of *ETFDH* and *EIF4EBP1* mRNA across both normal and tumor samples were obtained from The Cancer Genome Atlas (TCGA) and GTEx repositories. The expression data were normalized using the TMM (trimmed mean of M values) method and presented as log2 counts per million. Correlations between the genes were assessed using Pearson's correlation coefficient.

Quantification and Statistical Analysis

Statistical analysis was performed using GraphPad Prism 10. Data are presented as mean +/- SD of independent experiments, unless stated otherwise. Technical replicates were averaged from 2-

3 independent experiments. Details on data quantification, presentation, and statistical analysis are included in figure legends.

References

1. Kim, J., and DeBerardinis, R.J. (2019). Mechanisms and Implications of Metabolic Heterogeneity in Cancer. Cell Metab *30*, 434-446. 10.1016/j.cmet.2019.08.013.
2. Krieg, S., Fernandes, S.I., Kolliopoulos, C., Liu, M., and Fendt, S.M. (2024). Metabolic Signaling in Cancer Metastasis. Cancer Discov *14*, 934-952. 10.1158/2159-8290.CD-24-0174.
3. Faubert, B., Solmonson, A., and DeBerardinis, R.J. (2020). Metabolic reprogramming and cancer progression. Science *368*. 10.1126/science.aaw5473.
4. Hulea, L., Gravel, S.P., Morita, M., Cargnello, M., Uchenunu, O., Im, Y.K., Lehuede, C., Ma, E.H., Leibovitch, M., McLaughlan, S., et al. (2018). Translational and HIF-1alpha-Dependent Metabolic Reprogramming Underpin Metabolic Plasticity and Responses to Kinase Inhibitors and Biguanides. Cell Metab *28*, 817-832 e818. 10.1016/j.cmet.2018.09.001.
5. Vasan, K., Werner, M., and Chandel, N.S. (2020). Mitochondrial Metabolism as a Target for Cancer Therapy. Cell Metab *32*, 341-352. 10.1016/j.cmet.2020.06.019.
6. Banerjee, R., Purhonen, J., and Kallijarvi, J. (2022). The mitochondrial coenzyme Q junction and complex III: biochemistry and pathophysiology. FEBS J *289*, 6936-6958. 10.1111/febs.16164.
7. Mereis, M., Wanders, R.J.A., Schoonen, M., Dercksen, M., Smuts, I., and van der Westhuizen, F.H. (2021). Disorders of flavin adenine dinucleotide metabolism: MADD and related deficiencies. Int J Biochem Cell Biol *132*, 105899. 10.1016/j.biocel.2020.105899.
8. Ghisla, S., and Thorpe, C. (2004). Acyl-CoA dehydrogenases. A mechanistic overview. Eur J Biochem *271*, 494-508. 10.1046/j.1432-1033.2003.03946.x.
9. Zhang, Y., Mohsen, A.W., Kochersperger, C., Solo, K., Schmidt, A.V., Vockley, J., and Goetzman, E.S. (2019). An acyl-CoA dehydrogenase microplate activity assay using recombinant porcine electron transfer flavoprotein. Anal Biochem *581*, 113332. 10.1016/j.ab.2019.06.003.
10. El-Gharbawy, A., and Vockley, J. (2018). Inborn Errors of Metabolism with Myopathy: Defects of Fatty Acid Oxidation and the Carnitine Shuttle System. Pediatr Clin North Am *65*, 317-335. 10.1016/j.pcl.2017.11.006.
11. Herrero Martin, J.C., Salegi Ansa, B., Alvarez-Rivera, G., Dominguez-Zorita, S., Rodriguez-Pombo, P., Perez, B., Calvo, E., Paradela, A., Miguez, D.G., Cifuentes, A., et al. (2024). An ETFDH-driven metabolon supports OXPHOS efficiency in skeletal muscle by regulating coenzyme Q homeostasis. Nat Metab *6*, 209-225. 10.1038/s42255-023-00956-y.
12. Olsen, R.K., Olpin, S.E., Andresen, B.S., Miedzybrodzka, Z.H., Pourfarzam, M., Merinero, B., Frerman, F.E., Beresford, M.W., Dean, J.C., Cornelius, N., et al. (2007). ETFDH mutations as a major cause of riboflavin-responsive multiple acyl-CoA dehydrogenation deficiency. Brain *130*, 2045-2054. 10.1093/brain/awm135.

13. Missaglia, S., Tavian, D., and Angelini, C. (2021). ETF dehydrogenase advances in molecular genetics and impact on treatment. Crit Rev Biochem Mol Biol *56*, 360-372. 10.1080/10409238.2021.1908952.
14. Bertomeu, T., Coulombe-Huntington, J., Chatr-Aryamontri, A., Bourdages, K.G., Coyaud, E., Raught, B., Xia, Y., and Tyers, M. (2018). A High-Resolution Genome-Wide CRISPR/Cas9 Viability Screen Reveals Structural Features and Contextual Diversity of the Human Cell-Essential Proteome. Mol Cell Biol *38*. 10.1128/MCB.00302-17.
15. Ursini-Siegel, J., Hardy, W.R., Zuo, D., Lam, S.H., Sanguin-Gendreau, V., Cardiff, R.D., Pawson, T., and Muller, W.J. (2008). ShcA signalling is essential for tumour progression in mouse models of human breast cancer. EMBO J *27*, 910-920. 10.1038/emboj.2008.22.
16. Borowicz, S., Van Scoyk, M., Avasarala, S., Karuppusamy Rathinam, M.K., Tauler, J., Bikkavilli, R.K., and Winn, R.A. (2014). The soft agar colony formation assay. J Vis Exp, e51998. 10.3791/51998.
17. Szrok-Jurga, S., Czumaj, A., Turyn, J., Hebanowska, A., Swierczynski, J., Sledzinski, T., and Stelmanska, E. (2023). The Physiological and Pathological Role of Acyl-CoA Oxidation. Int J Mol Sci *24*. 10.3390/ijms241914857.
18. DeBerardinis, R.J., and Cheng, T. (2010). Q's next: the diverse functions of glutamine in metabolism, cell biology and cancer. Oncogene *29*, 313-324. 10.1038/onc.2009.358.
19. Saxton, R.A., and Sabatini, D.M. (2017). mTOR Signaling in Growth, Metabolism, and Disease. Cell *168*, 960-976. 10.1016/j.cell.2017.02.004.
20. Thoreen, C.C., Kang, S.A., Chang, J.W., Liu, Q., Zhang, J., Gao, Y., Reichling, L.J., Sim, T., Sabatini, D.M., and Gray, N.S. (2009). An ATP-competitive mammalian target of rapamycin inhibitor reveals rapamycin-resistant functions of mTORC1. J Biol Chem *284*, 8023-8032. 10.1074/jbc.M900301200.
21. Lee, B.J., Boyer, J.A., Burnett, G.L., Thottumkara, A.P., Tibrewal, N., Wilson, S.L., Hsieh, T., Marquez, A., Lorenzana, E.G., Evans, J.W., et al. (2021). Selective inhibitors of mTORC1 activate 4EBP1 and suppress tumor growth. Nat Chem Biol *17*, 1065-1074. 10.1038/s41589-021-00813-7.
22. Harding, H.P., Novoa, I., Zhang, Y., Zeng, H., Wek, R., Schapira, M., and Ron, D. (2000). Regulated translation initiation controls stress-induced gene expression in mammalian cells. Mol Cell *6*, 1099-1108. 10.1016/s1097-2765(00)00108-8.
23. Dowling, R.J., Topisirovic, I., Alain, T., Bidinosti, M., Fonseca, B.D., Petroulakis, E., Wang, X., Larsson, O., Selvaraj, A., Liu, Y., et al. (2010). mTORC1-mediated cell proliferation, but not cell growth, controlled by the 4E-BPs. Science *328*, 1172-1176. 10.1126/science.1187532.
24. Gingras, A.C., Gygi, S.P., Raught, B., Polakiewicz, R.D., Abraham, R.T., Hoekstra, M.F., Aebersold, R., and Sonenberg, N. (1999). Regulation of 4E-BP1 phosphorylation: a novel two-step mechanism. Genes Dev *13*, 1422-1437. 10.1101/gad.13.11.1422.
25. Morita, M., Gravel, S.P., Chenard, V., Sikstrom, K., Zheng, L., Alain, T., Gandin, V., Avizonis, D., Arguello, M., Zakaria, C., et al. (2013). mTORC1 controls mitochondrial activity and biogenesis through 4E-BP-dependent translational regulation. Cell Metab *18*, 698-711. 10.1016/j.cmet.2013.10.001.
26. Morita, M., Gravel, S.P., Hulea, L., Larsson, O., Pollak, M., St-Pierre, J., and Topisirovic, I. (2015). mTOR coordinates protein synthesis, mitochondrial activity and proliferation. Cell Cycle *14*, 473-480. 10.4161/15384101.2014.991572.
27. Yamaguchi, S., Ishihara, H., Yamada, T., Tamura, A., Usui, M., Tominaga, R., Munakata, Y., Satake, C., Katagiri, H., Tashiro, F., et al. (2008). ATF4-mediated induction of 4E-BP1

contributes to pancreatic beta cell survival under endoplasmic reticulum stress. Cell Metab *7*, 269-276. 10.1016/j.cmet.2008.01.008.

28. Wang, J., Ye, Q., Cao, Y., Guo, Y., Huang, X., Mi, W., Liu, S., Wang, C., Yang, H.S., Zhou, B.P., et al. (2017). Snail determines the therapeutic response to mTOR kinase inhibitors by transcriptional repression of 4E-BP1. Nat Commun *8*, 2207. 10.1038/s41467-017-02243-3.
29. Totten, S.P., Im, Y.K., Cepeda Canedo, E., Najyb, O., Nguyen, A., Hebert, S., Ahn, R., Lewis, K., Lebeau, B., La Selva, R., et al. (2021). STAT1 potentiates oxidative stress revealing a targetable vulnerability that increases phenformin efficacy in breast cancer. Nat Commun *12*, 3299. 10.1038/s41467-021-23396-2.
30. Hayes, J.D., Dinkova-Kostova, A.T., and Tew, K.D. (2020). Oxidative Stress in Cancer. Cancer Cell *38*, 167-197. 10.1016/j.ccell.2020.06.001.
31. Nakayamada, S., Poholek, A.C., Lu, K.T., Takahashi, H., Kato, M., Iwata, S., Hirahara, K., Cannons, J.L., Schwartzberg, P.L., Vahedi, G., et al. (2014). Type I IFN induces binding of STAT1 to Bcl6: divergent roles of STAT family transcription factors in the T follicular helper cell genetic program. J Immunol *192*, 2156-2166. 10.4049/jimmunol.1300675.
32. Liu, Y., Feng, J., Yuan, K., Wu, Z., Hu, L., Lu, Y., Li, K., Guo, J., Chen, J., Ma, C., and Pang, X. (2022). The oncoprotein BCL6 enables solid tumor cells to evade genotoxic stress. Elife *11*. 10.7554/eLife.69255.
33. Madapura, H.S., Nagy, N., Ujvari, D., Kallas, T., Krohnke, M.C.L., Amu, S., Bjorkholm, M., Stenke, L., Mandal, P.K., McMurray, J.S., et al. (2017). Interferon gamma is a STAT1-dependent direct inducer of BCL6 expression in imatinib-treated chronic myeloid leukemia cells. Oncogene *36*, 4619-4628. 10.1038/onc.2017.85.
34. Ramachandran, K., Futtner, C.R., Sommars, M.A., Quattrocelli, M., Omura, Y., Fruzyna, E., Wang, J.C., Waldeck, N.J., Senagolage, M.D., Telles, C.G., et al. (2024). Transcriptional programming of translation by BCL6 controls skeletal muscle proteostasis. Nat Metab *6*, 304-322. 10.1038/s42255-024-00983-3.
35. Yi, W., Gupta, S., Ricker, E., Manni, M., Jessberger, R., Chinenov, Y., Molina, H., and Pernis, A.B. (2017). The mTORC1-4E-BP-eIF4E axis controls de novo Bcl6 protein synthesis in T cells and systemic autoimmunity. Nat Commun *8*, 254. 10.1038/s41467-017-00348-3.
36. Xu, L., Huang, Q., Wang, H., Hao, Y., Bai, Q., Hu, J., Li, Y., Wang, P., Chen, X., He, R., et al. (2017). The Kinase mTORC1 Promotes the Generation and Suppressive Function of Follicular Regulatory T Cells. Immunity *47*, 538-551 e535. 10.1016/j.immuni.2017.08.011.
37. Raybuck, A.L., Cho, S.H., Li, J., Rogers, M.C., Lee, K., Williams, C.L., Shlomchik, M., Thomas, J.W., Chen, J., Williams, J.V., and Boothby, M.R. (2018). B Cell-Intrinsic mTORC1 Promotes Germinal Center-Defining Transcription Factor Gene Expression, Somatic Hypermutation, and Memory B Cell Generation in Humoral Immunity. J Immunol *200*, 2627-2639. 10.4049/jimmunol.1701321.
38. Consortium, I.T.P.-C.A.o.W.G. (2020). Pan-cancer analysis of whole genomes. Nature *578*, 82-93. 10.1038/s41586-020-1969-6.
39. Powell, G., Pavlovic Djuranovic, S., and Djuranovic, S. (2021). Gene dosage effects of poly(A) track-engineered hypomorphs. Mol Ther Nucleic Acids *26*, 865-878. 10.1016/j.omtn.2021.10.005.

40. Arthur, L., Pavlovic-Djuranovic, S., Smith-Koutmou, K., Green, R., Szczesny, P., and Djuranovic, S. (2015). Translational control by lysine-encoding A-rich sequences. Sci Adv *1*. 10.1126/sciadv.1500154.
41. Jumper, J., Evans, R., Pritzel, A., Green, T., Figurnov, M., Ronneberger, O., Tunyasuvunakool, K., Bates, R., Zidek, A., Potapenko, A., et al. (2021). Highly accurate protein structure prediction with AlphaFold. Nature *596*, 583-589. 10.1038/s41586-021-03819-2.
42. Varadi, M., Anyango, S., Deshpande, M., Nair, S., Natassia, C., Yordanova, G., Yuan, D., Stroe, O., Wood, G., Laydon, A., et al. (2022). AlphaFold Protein Structure Database: massively expanding the structural coverage of protein-sequence space with high-accuracy models. Nucleic Acids Res *50*, D439-D444. 10.1093/nar/gkab1061.
43. Jones, P.A., and Baylin, S.B. (2002). The fundamental role of epigenetic events in cancer. Nat Rev Genet *3*, 415-428. 10.1038/nrg816.
44. Mossmann, D., Park, S., and Hall, M.N. (2018). mTOR signalling and cellular metabolism are mutual determinants in cancer. Nat Rev Cancer *18*, 744-757. 10.1038/s41568-018-0074-8.
45. Iadevaia, V., Liu, R., and Proud, C.G. (2014). mTORC1 signaling controls multiple steps in ribosome biogenesis. Semin Cell Dev Biol *36*, 113-120. 10.1016/j.semcdb.2014.08.004.
46. Papadopoli, D., Boulay, K., Kazak, L., Pollak, M., Mallette, F., Topisirovic, I., and Hulea, L. (2019). mTOR as a central regulator of lifespan and aging. F1000Res *8*. 10.12688/f1000research.17196.1.
47. Morita, M., Prudent, J., Basu, K., Goyon, V., Katsumura, S., Hulea, L., Pearl, D., Siddiqui, N., Strack, S., McGuirk, S., et al. (2017). mTOR Controls Mitochondrial Dynamics and Cell Survival via MTFP1. Mol Cell *67*, 922-935 e925. 10.1016/j.molcel.2017.08.013.
48. So, L., Lee, J., Palafox, M., Mallya, S., Woxland, C.G., Arguello, M., Truitt, M.L., Sonenberg, N., Ruggero, D., and Fruman, D.A. (2016). The 4E-BP-eIF4E axis promotes rapamycin-sensitive growth and proliferation in lymphocytes. Sci Signal *9*, ra57. 10.1126/scisignal.aad8463.
49. Polunovsky, V.A., Gingras, A.C., Sonenberg, N., Peterson, M., Tan, A., Rubins, J.B., Manivel, J.C., and Bitterman, P.B. (2000). Translational control of the antiapoptotic function of Ras. J Biol Chem *275*, 24776-24780. 10.1074/jbc.M001938200.
50. Lynch, M., Fitzgerald, C., Johnston, K.A., Wang, S., and Schmidt, E.V. (2004). Activated eIF4E-binding protein slows G1 progression and blocks transformation by c-myc without inhibiting cell growth. J Biol Chem *279*, 3327-3339. 10.1074/jbc.M310872200.
51. Avdulov, S., Li, S., Michalek, V., Burrichter, D., Peterson, M., Perlman, D.M., Manivel, J.C., Sonenberg, N., Yee, D., Bitterman, P.B., and Polunovsky, V.A. (2004). Activation of translation complex eIF4F is essential for the genesis and maintenance of the malignant phenotype in human mammary epithelial cells. Cancer Cell *5*, 553-563. 10.1016/j.ccr.2004.05.024.
52. Deslypere, J.P., and Vermeulen, A. (1991). Rhabdomyolysis and simvastatin. Ann Intern Med *114*, 342. 10.7326/0003-4819-114-4-342_1.
53. Rousseau, D., Gingras, A.C., Pause, A., and Sonenberg, N. (1996). The eIF4E-binding proteins 1 and 2 are negative regulators of cell growth. Oncogene *13*, 2415-2420.
54. Musa, J., Orth, M.F., Dallmayer, M., Baldauf, M., Pardo, C., Rotblat, B., Kirchner, T., Leprivier, G., and Grunewald, T.G. (2016). Eukaryotic initiation factor 4E-binding protein 1 (4E-BP1): a master regulator of mRNA translation involved in tumorigenesis. Oncogene *35*, 4675-4688. 10.1038/onc.2015.515.

55. Jewer, M., Lee, L., Leibovitch, M., Zhang, G., Liu, J., Findlay, S.D., Vincent, K.M., Tandoc, K., Dieters-Castator, D., Quail, D.F., et al. (2020). Translational control of breast cancer plasticity. Nat Commun *11*, 2498. 10.1038/s41467-020-16352-z.
56. Teleman, A.A., Chen, Y.W., and Cohen, S.M. (2005). 4E-BP functions as a metabolic brake used under stress conditions but not during normal growth. Genes Dev *19*, 1844-1848. 10.1101/gad.341505.
57. Levy, T., Voeltzke, K., Hruby, L., Alasad, K., Bas, Z., Snaebjornsson, M., Marciano, R., Scharov, K., Planque, M., Vriens, K., et al. (2024). mTORC1 regulates cell survival under glucose starvation through 4EBP1/2-mediated translational reprogramming of fatty acid metabolism. Nat Commun *15*, 4083. 10.1038/s41467-024-48386-y.
58. Fernando, T.M., Marullo, R., Pera Gresely, B., Phillip, J.M., Yang, S.N., Lundell-Smith, G., Torregroza, I., Ahn, H., Evans, T., Gyorffy, B., et al. (2019). BCL6 Evolved to Enable Stress Tolerance in Vertebrates and Is Broadly Required by Cancer Cells to Adapt to Stress. Cancer Discov *9*, 662-679. 10.1158/2159-8290.CD-17-1444.
59. Chen, D., Zang, Y.H., Qiu, Y., Zhang, F., Chen, A.D., Wang, J.J., Chen, Q., Li, Y.H., Kang, Y.M., and Zhu, G.Q. (2019). BCL6 Attenuates Proliferation and Oxidative Stress of Vascular Smooth Muscle Cells in Hypertension. Oxid Med Cell Longev *2019*, 5018410. 10.1155/2019/5018410.
60. Oestreich, K.J., Read, K.A., Gilbertson, S.E., Hough, K.P., McDonald, P.W., Krishnamoorthy, V., and Weinmann, A.S. (2014). Bcl-6 directly represses the gene program of the glycolysis pathway. Nat Immunol *15*, 957-964. 10.1038/ni.2985.
61. Senagolage, M.D., Sommars, M.A., Ramachandran, K., Futtner, C.R., Omura, Y., Allred, A.L., Wang, J., Yang, C., Procissi, D., Evans, R.M., et al. (2018). Loss of Transcriptional Repression by BCL6 Confers Insulin Sensitivity in the Setting of Obesity. Cell Rep *25*, 3283-3298 e3286. 10.1016/j.celrep.2018.11.074.
62. McLachlan, T., Matthews, W.C., Jackson, E.R., Staudt, D.E., Douglas, A.M., Findlay, I.J., Persson, M.L., Duchatel, R.J., Mannan, A., Germon, Z.P., and Dun, M.D. (2022). B-cell Lymphoma 6 (BCL6): From Master Regulator of Humoral Immunity to Oncogenic Driver in Pediatric Cancers. Mol Cancer Res *20*, 1711-1723. 10.1158/1541-7786.MCR-22-0567.
63. Nilsson, R., Jain, M., Madhusudhan, N., Sheppard, N.G., Strittmatter, L., Kampf, C., Huang, J., Asplund, A., and Mootha, V.K. (2014). Metabolic enzyme expression highlights a key role for MTHFD2 and the mitochondrial folate pathway in cancer. Nat Commun *5*, 3128. 10.1038/ncomms4128.
64. Smith, H.W., Hirukawa, A., Sanguin-Gendreau, V., Nandi, I., Dufour, C.R., Zuo, D., Tandoc, K., Leibovitch, M., Singh, S., Rennhack, J.P., et al. (2019). An ErbB2/c-Src axis links bioenergetics with PRC2 translation to drive epigenetic reprogramming and mammary tumorigenesis. Nat Commun *10*, 2901. 10.1038/s41467-019-10681-4.
65. Harachi, M., Masui, K., Honda, H., Muragaki, Y., Kawamata, T., Cavenee, W.K., Mischel, P.S., and Shibata, N. (2020). Dual Regulation of Histone Methylation by mTOR Complexes Controls Glioblastoma Tumor Cell Growth via EZH2 and SAM. Mol Cancer Res *18*, 1142-1152. 10.1158/1541-7786.MCR-20-0024.
66. Chen, M., Fang, Y., Liang, M., Zhang, N., Zhang, X., Xu, L., Ren, X., Zhang, Q., Zhou, Y., Peng, S., et al. (2023). The activation of mTOR signalling modulates DNA methylation by enhancing DNMT1 translation in hepatocellular carcinoma. J Transl Med *21*, 276. 10.1186/s12967-023-04103-9.
67. Kim, H., Lebeau, B., Papadopoli, D., Jovanovic, P., Russo, M., Avizonis, D., Morita, M., Afzali, F., Ursini-Siegel, J., Postovit, L.-M., et al. (2023). MTOR modulation induces

selective perturbations in histone methylation which influence the anti-proliferative effects of mTOR inhibitors. bioRxiv, 2023.2011.2007.566067. 10.1101/2023.11.07.566067.
68. Wolfson, R.L., and Sabatini, D.M. (2017). The Dawn of the Age of Amino Acid Sensors for the mTORC1 Pathway. Cell Metab *26*, 301-309. 10.1016/j.cmet.2017.07.001.
69. Hesketh, G.G., Papazotos, F., Pawling, J., Rajendran, D., Knight, J.D.R., Martinez, S., Taipale, M., Schramek, D., Dennis, J.W., and Gingras, A.C. (2020). The GATOR-Rag GTPase pathway inhibits mTORC1 activation by lysosome-derived amino acids. Science *370*, 351-356. 10.1126/science.aaz0863.
70. Cerami, E., Gao, J., Dogrusoz, U., Gross, B.E., Sumer, S.O., Aksoy, B.A., Jacobsen, A., Byrne, C.J., Heuer, M.L., Larsson, E., et al. (2012). The cBio cancer genomics portal: an open platform for exploring multidimensional cancer genomics data. Cancer Discov *2*, 401-404. 10.1158/2159-8290.CD-12-0095.
71. Gao, J., Aksoy, B.A., Dogrusoz, U., Dresdner, G., Gross, B., Sumer, S.O., Sun, Y., Jacobsen, A., Sinha, R., Larsson, E., et al. (2013). Integrative analysis of complex cancer genomics and clinical profiles using the cBioPortal. Sci Signal *6*, pl1. 10.1126/scisignal.2004088.
72. de Bruijn, I., Kundra, R., Mastrogiacomo, B., Tran, T.N., Sikina, L., Mazor, T., Li, X., Ochoa, A., Zhao, G., Lai, B., et al. (2023). Analysis and Visualization of Longitudinal Genomic and Clinical Data from the AACR Project GENIE Biopharma Collaborative in cBioPortal. Cancer Res *83*, 3861-3867. 10.1158/0008-5472.CAN-23-0816.
73. Rose, A.A., Pepin, F., Russo, C., Abou Khalil, J.E., Hallett, M., and Siegel, P.M. (2007). Osteoactivin promotes breast cancer metastasis to bone. Mol Cancer Res *5*, 1001-1014. 10.1158/1541-7786.MCR-07-0119.
74. Labun, K., Montague, T.G., Krause, M., Torres Cleuren, Y.N., Tjeldnes, H., and Valen, E. (2019). CHOPCHOP v3: expanding the CRISPR web toolbox beyond genome editing. Nucleic Acids Res *47*, W171-W174. 10.1093/nar/gkz365.
75. Sanjana, N.E., Shalem, O., and Zhang, F. (2014). Improved vectors and genome-wide libraries for CRISPR screening. Nat Methods *11*, 783-784. 10.1038/nmeth.3047.
76. Shalem, O., Sanjana, N.E., Hartenian, E., Shi, X., Scott, D.A., Mikkelson, T., Heckl, D., Ebert, B.L., Root, D.E., Doench, J.G., and Zhang, F. (2014). Genome-scale CRISPR-Cas9 knockout screening in human cells. Science *343*, 84-87. 10.1126/science.1247005.
77. Papadopoli, D., Uchenunu, O., Palia, R., Chekkal, N., Hulea, L., Topisirovic, I., Pollak, M., and St-Pierre, J. (2021). Perturbations of cancer cell metabolism by the antidiabetic drug canagliflozin. Neoplasia *23*, 391-399. 10.1016/j.neo.2021.02.003.
78. Tabaries, S., Annis, M.G., Lazaris, A., Petrillo, S.K., Huxham, J., Abdellatif, A., Palmieri, V., Chabot, J., Johnson, R.M., Van Laere, S., et al. (2021). Claudin-2 promotes colorectal cancer liver metastasis and is a biomarker of the replacement type growth pattern. Commun Biol *4*, 657. 10.1038/s42003-021-02189-9.
79. Igelmann, S., Lessard, F., Uchenunu, O., Bouchard, J., Fernandez-Ruiz, A., Rowell, M.C., Lopes-Paciencia, S., Papadopoli, D., Fouillen, A., Ponce, K.J., et al. (2021). A hydride transfer complex reprograms NAD metabolism and bypasses senescence. Mol Cell *81*, 3848-3865 e3819. 10.1016/j.molcel.2021.08.028.
80. Gandin, V., Sikstrom, K., Alain, T., Morita, M., McLaughlan, S., Larsson, O., and Topisirovic, I. (2014). Polysome fractionation and analysis of mammalian translatomes on a genome-wide scale. J Vis Exp. 10.3791/51455.

81. McGuirk, S., Gravel, S.P., Deblois, G., Papadopoli, D.J., Faubert, B., Wegner, A., Hiller, K., Avizonis, D., Akavia, U.D., Jones, R.G., et al. (2013). PGC-1alpha supports glutamine metabolism in breast cancer. Cancer Metab *1*, 22. 10.1186/2049-3002-1-22.
82. Mookerjee, S.A., Gerencser, A.A., Nicholls, D.G., and Brand, M.D. (2017). Quantifying intracellular rates of glycolytic and oxidative ATP production and consumption using extracellular flux measurements. J Biol Chem *292*, 7189-7207. 10.1074/jbc.M116.774471.
83. Topisirovic, I., Siddiqui, N., Orolicki, S., Skrabanek, L.A., Tremblay, M., Hoang, T., and Borden, K.L. (2009). Stability of eukaryotic translation initiation factor 4E mRNA is regulated by HuR, and this activity is dysregulated in cancer. Mol Cell Biol *29*, 1152-1162. 10.1128/MCB.01532-08.

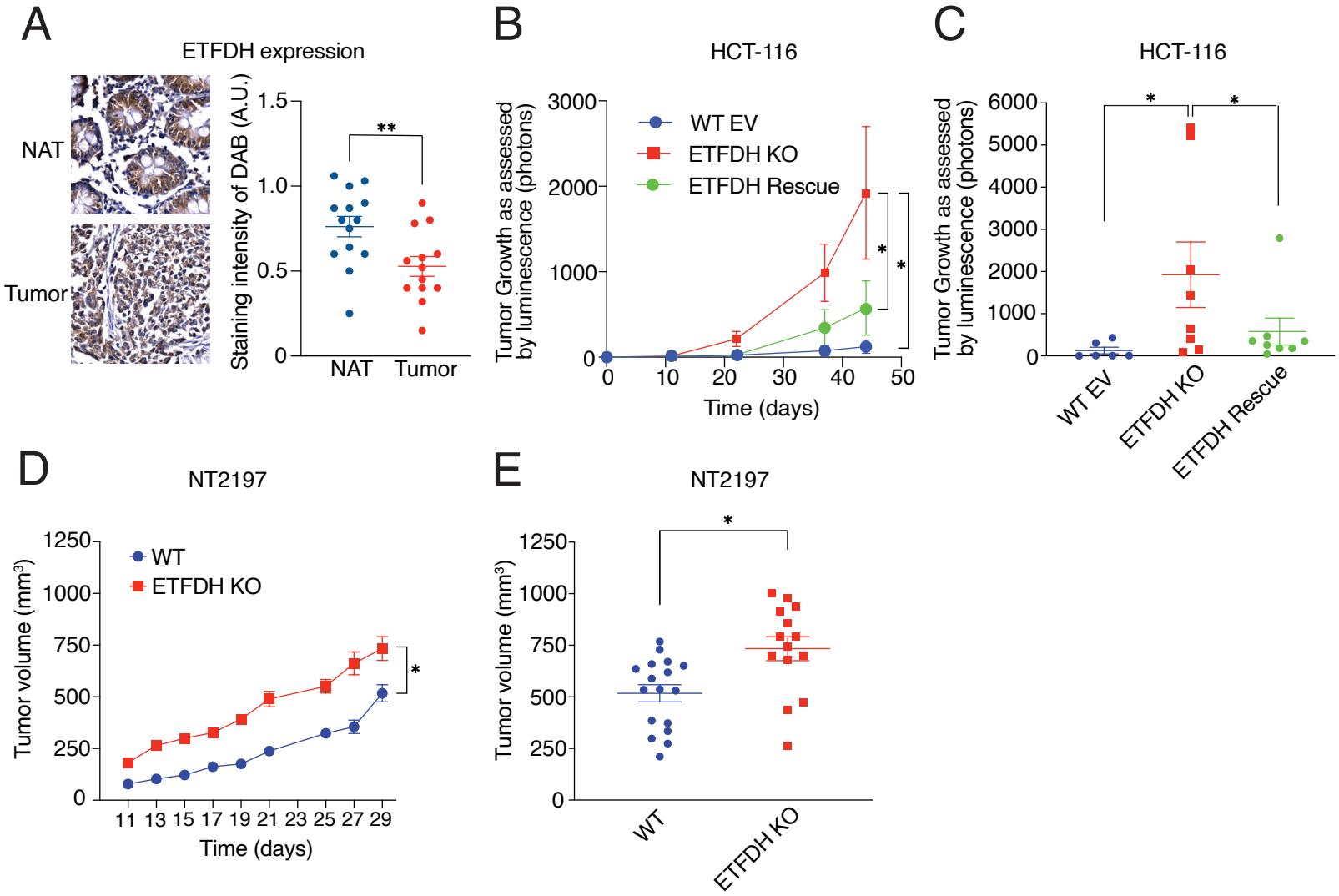
A
ETFDH expression
NAT
Tumor
Staining intensity of DAB (A.U.)
1.5
1.0
0.5
0
**
NAT
Tumor
B
HCT-116
Tumor Growth as assessed by luminescence (photons)
3000
2000
1000
0
WT EV
ETFDH KO
ETFDH Rescue
*
*
0
10
20
30
40
50
Time (days)
C
HCT-116
Tumor Growth as assessed by luminescence (photons)
6000
5000
4000
3000
2000
1000
0
*
*
WT EV
ETFDH KO
ETFDH Rescue
D
NT2197
Tumor volume (mm3)
1250
1000
750
500
250
0
WT
ETFDH KO
*
11 13 15 17 19 21 23 25 27 29
Time (days)
E
NT2197
Tumor volume (mm3)
1250
1000
750
500
250
0
*
WT
ETFDH KO

Fig.1

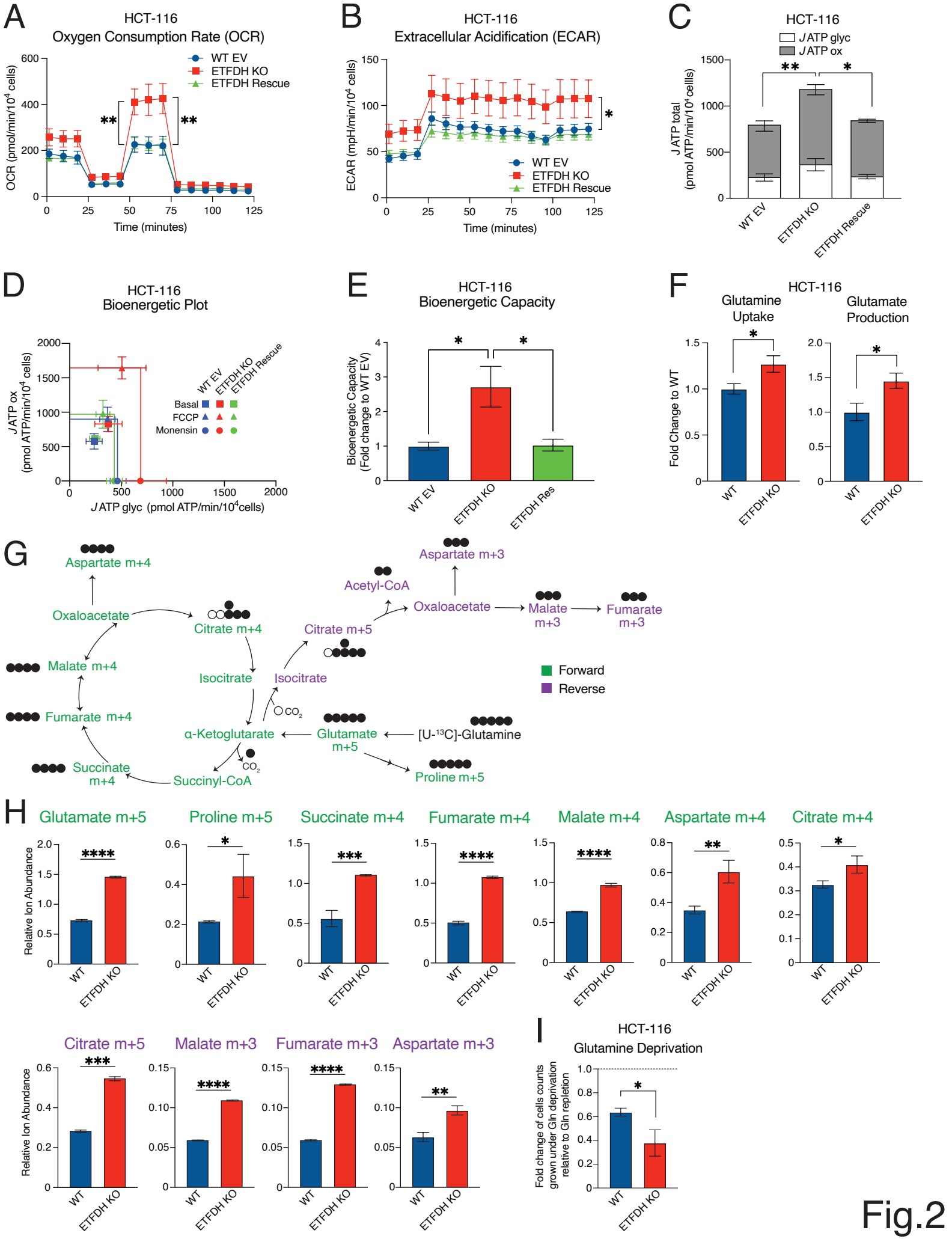
A
HCT-116
Oxygen Consumption Rate (OCR)
WT EV
ETFDH KO
ETFDH Rescue
OCR (pmol/min/10^4 cells)
Time (minutes)
B
HCT-116
Extracellular Acidification (ECAR)
ECAR (mpH/min/10^4 cells)
Time (minutes)
C
HCT-116
J ATP glyc
J ATP ox
J ATP total (pmol ATP/min/10^4 cells)
WT EV
ETFDH KO
ETFDH Rescue
D
HCT-116
Bioenergetic Plot
J ATP ox (pmol ATP/min/10^4 cells)
J ATP glyc (pmol ATP/min/10^4cells)
Basal
FCCP
Monensin
E
HCT-116
Bioenergetic Capacity
Bioenergetic Capacity (Fold change to WT EV)
WT EV
ETFDH KO
ETFDH Res
F
HCT-116
Glutamine Uptake
Glutamate Production
Fold Change to WT
WT
ETFDH KO
G
Aspartate m+4
Oxaloacetate
Citrate m+4
Malate m+4
Isocitrate
Fumarate m+4
α-Ketoglutarate
Succinate m+4
Succinyl-CoA
Citrate m+5
Isocitrate
Acetyl-CoA
Aspartate m+3
Oxaloacetate
Malate m+3
Fumarate m+3
Glutamate m+5
[U-13C]-Glutamine
Proline m+5
Forward
Reverse
H
Glutamate m+5
Proline m+5
Succinate m+4
Fumarate m+4
Malate m+4
Aspartate m+4
Citrate m+4
Citrate m+5
Malate m+3
Fumarate m+3
Aspartate m+3
Relative Ion Abundance
WT
ETFDH KO
I
HCT-116
Glutamine Deprivation
Fold change of cells counts grown under Gln deprivation relative to Gln repletion
WT
ETFDH KO

Fig.2

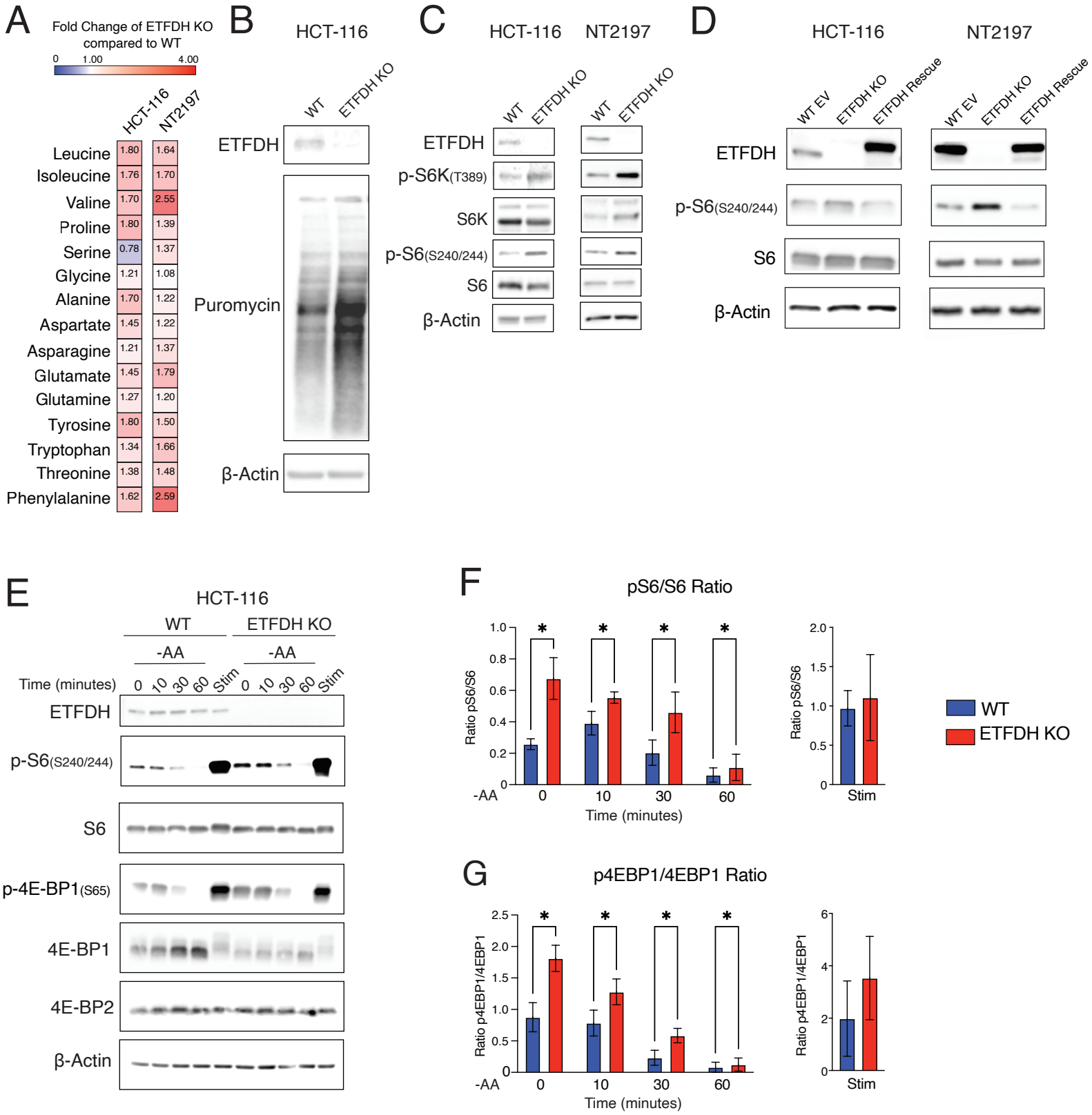
A
Fold Change of ETFDH KO compared to WT
0
1.00
4.00
HCT-116
NT2197
Leucine 1.80 1.64
Isoleucine 1.76 1.70
Valine 1.70 2.55
Proline 1.80 1.39
Serine 0.78 1.37
Glycine 1.21 1.08
Alanine 1.70 1.22
Aspartate 1.45 1.22
Asparagine 1.21 1.37
Glutamate 1.45 1.79
Glutamine 1.27 1.20
Tyrosine 1.80 1.50
Tryptophan 1.34 1.66
Threonine 1.38 1.48
Phenylalanine 1.62 2.59
B
HCT-116
WT
ETFDH KO
ETFDH
Puromycin
β-Actin
C
HCT-116
NT2197
WT
ETFDH KO
ETFDH
p-S6K(T389)
S6K
p-S6(S240/244)
S6
β-Actin
D
HCT-116
NT2197
WT EV
ETFDH KO
ETFDH Rescue
ETFDH
p-S6(S240/244)
S6
β-Actin
E
HCT-116
WT
ETFDH KO
-AA
Time (minutes)
0
10
30
60
Stim
ETFDH
p-S6(S240/244)
S6
p-4E-BP1(S65)
4E-BP1
4E-BP2
β-Actin
F
pS6/S6 Ratio
Ratio pS6/S6
-AA
Time (minutes)
Stim
WT
ETFDH KO
G
p4EBP1/4EBP1 Ratio
Ratio p4EBP1/4EBP1

Fig.3

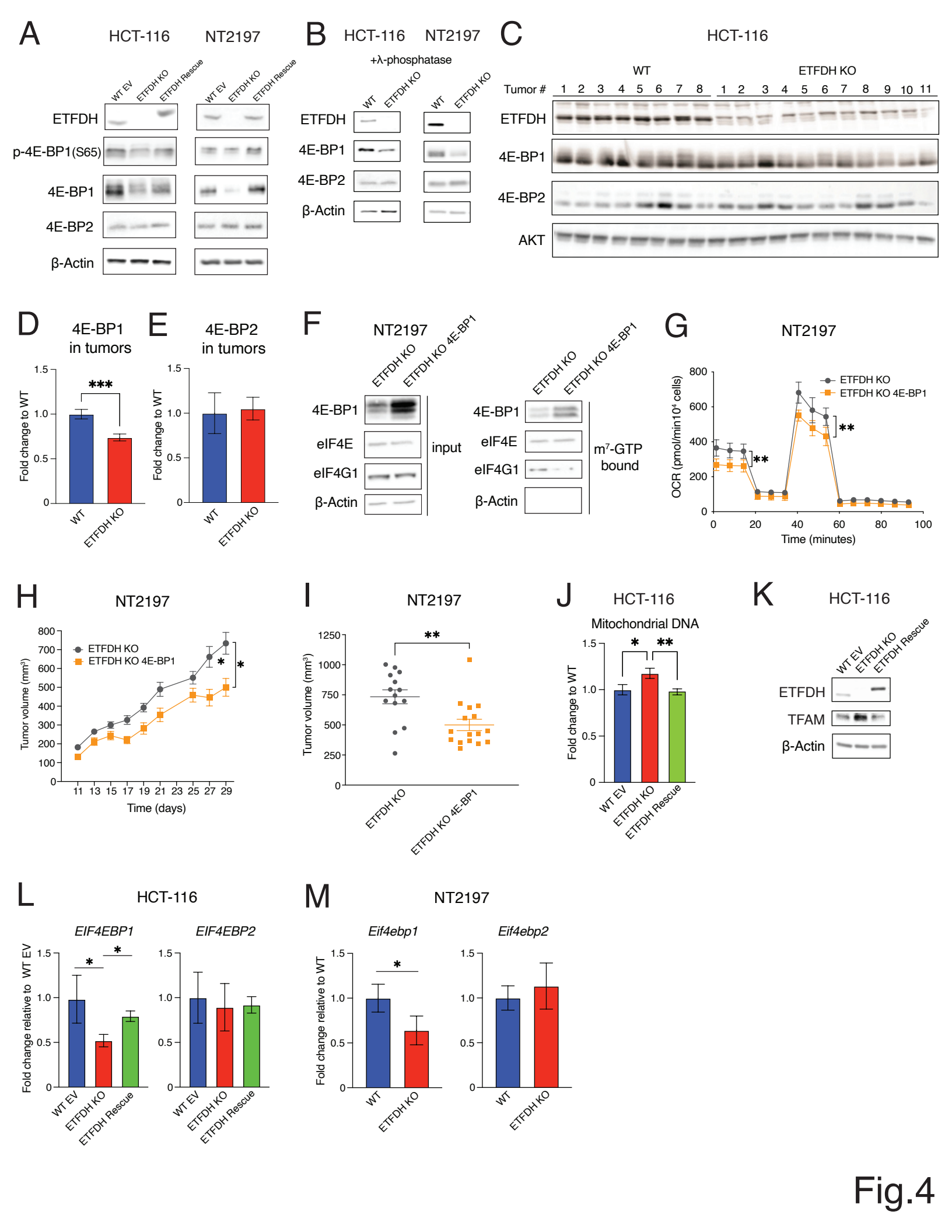
A
HCT-116
NT2197
WT EV
ETFDH KO
ETFDH Rescue
ETFDH
p-4E-BP1(S65)
4E-BP1
4E-BP2
β-Actin
B
HCT-116
NT2197
+λ-phosphatase
WT
ETFDH KO
ETFDH
4E-BP1
4E-BP2
β-Actin
C
HCT-116
WT
ETFDH KO
Tumor #
1 2 3 4 5 6 7 8
1 2 3 4 5 6 7 8 9 10 11
ETFDH
4E-BP1
4E-BP2
AKT
D
4E-BP1
in tumors
Fold change to WT
***
WT
ETFDH KO
E
4E-BP2
in tumors
Fold change to WT
WT
ETFDH KO
F
NT2197
ETFDH KO
ETFDH KO 4E-BP1
4E-BP1
eIF4E
eIF4G1
β-Actin
input
m7-GTP
bound
G
NT2197
ETFDH KO
ETFDH KO 4E-BP1
OCR (pmol/min10⁴ cells)
Time (minutes)
**
H
NT2197
ETFDH KO
ETFDH KO 4E-BP1
Tumor volume (mm³)
Time (days)
*
I
NT2197
Tumor volume (mm³)
**
ETFDH KO
ETFDH KO 4E-BP1
J
HCT-116
Mitochondrial DNA
Fold change to WT
WT EV
ETFDH KO
ETFDH Rescue
K
HCT-116
WT EV
ETFDH KO
ETFDH Rescue
ETFDH
TFAM
β-Actin
L
HCT-116
EIF4EBP1
EIF4EBP2
Fold change relative to WT EV
WT EV
ETFDH KO
ETFDH Rescue
M
NT2197
Eif4ebp1
Eif4ebp2
Fold change relative to WT
WT
ETFDH KO

Fig.4

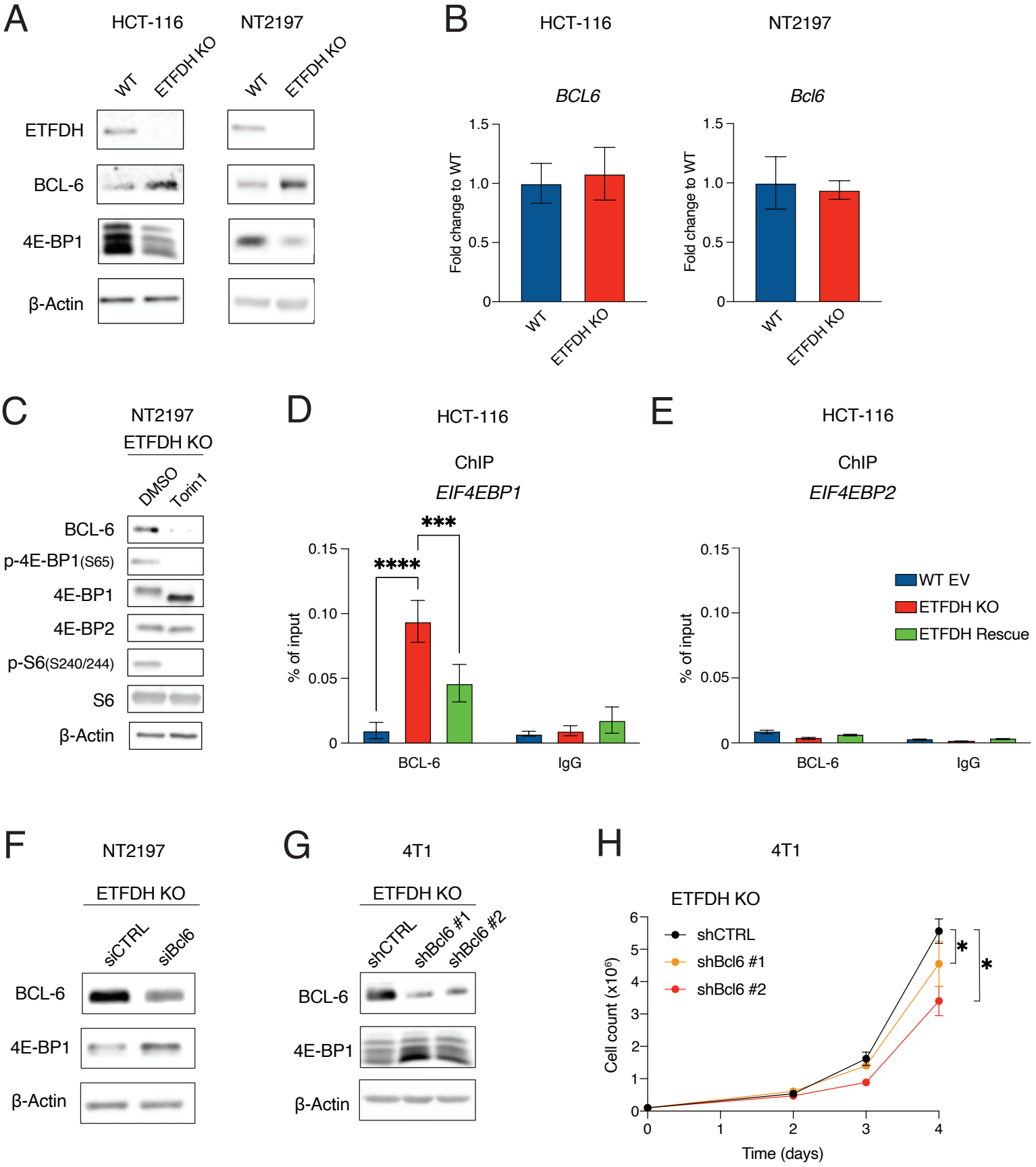
A
HCT-116
NT2197
WT
ETFDH KO
WT
ETFDH KO
ETFDH
BCL-6
4E-BP1
β-Actin
B
HCT-116
NT2197
BCL6
Bcl6
Fold change to WT
1.5
1.0
0.5
0
WT
ETFDH KO
C
NT2197
ETFDH KO
DMSO
Torin1
BCL-6
p-4E-BP1(S65)
4E-BP1
4E-BP2
p-S6(S240/244)
S6
β-Actin
D
HCT-116
ChIP
EIF4EBP1
% of input
0.15
0.10
0.05
0
****
***
BCL-6
IgG
E
HCT-116
ChIP
EIF4EBP2
% of input
0.15
0.10
0.05
0
WT EV
ETFDH KO
ETFDH Rescue
BCL-6
IgG
F
NT2197
ETFDH KO
siCTRL
siBcl6
BCL-6
4E-BP1
β-Actin
G
4T1
ETFDH KO
shCTRL
shBcl6 #1
shBcl6 #2
BCL-6
4E-BP1
β-Actin
H
4T1
ETFDH KO
shCTRL
shBcl6 #1
shBcl6 #2
Cell count (x10⁶)
6
5
4
3
2
1
0
*
*
0
1
2
3
4
Time (days)

Fig.5

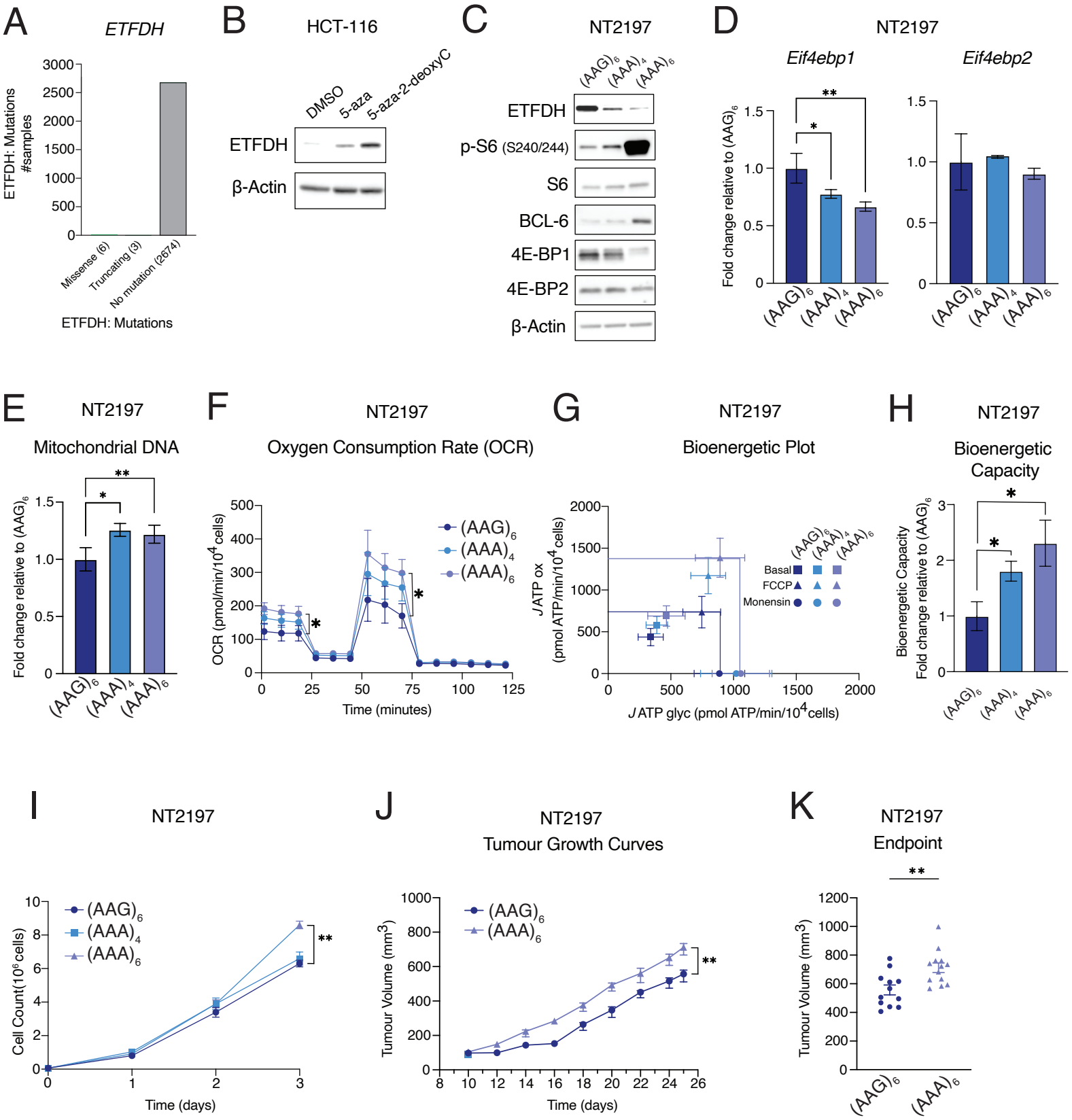
A
ETFDH
ETFDH: Mutations #samples
3000
2500
2000
1500
1000
500
0
Missense (6)
Truncating (3)
No mutation (2674)
ETFDH: Mutations
B
HCT-116
DMSO
5-aza
5-aza-2-deoxyC
ETFDH
β-Actin
C
NT2197
(AAG)6
(AAA)4
(AAA)6
ETFDH
p-S6 (S240/244)
S6
BCL-6
4E-BP1
4E-BP2
β-Actin
D
NT2197
Eif4ebp1
Eif4ebp2
Fold change relative to (AAG)6
E
NT2197
Mitochondrial DNA
Fold change relative to (AAG)6
F
NT2197
Oxygen Consumption Rate (OCR)
OCR (pmol/min/10^4 cells)
Time (minutes)
G
NT2197
Bioenergetic Plot
J ATP ox (pmol ATP/min/10^4 cells)
J ATP glyc (pmol ATP/min/10^4 cells)
Basal
FCCP
Monensin
H
NT2197
Bioenergetic Capacity
Bioenergetic Capacity
Fold change relative to (AAG)6
I
NT2197
Cell Count(10^6 cells)
Time (days)
J
NT2197
Tumour Growth Curves
Tumour Volume (mm^3)
Time (days)
K
NT2197
Endpoint
Tumour Volume (mm^3)

Fig.6

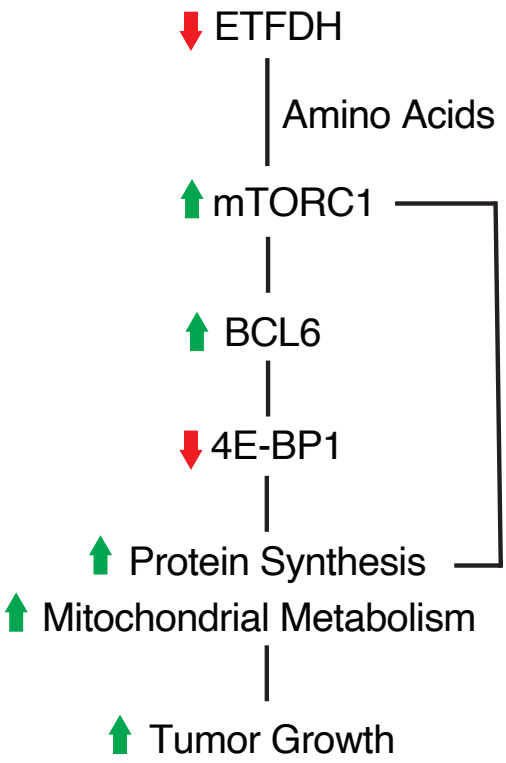
ETFDH
Amino Acids
mTORC1
BCL6
4E-BP1
Protein Synthesis
Mitochondrial Metabolism
Tumor Growth

Fig.7